Journal of Vibration Engineering & Technologies (2025) 13:413
https://doi.org/10.1007/s42417-025-01967-7

ORIGINAL PAPER

Hybrid Piezoelectric-Electromagnetic Cut-Out Energy Harvester with Adaptive Potential Wells: Design and Nonlinear Modeling

Yasaman Ghalami[1] · **Amir R. Askari**[2,3] · **Masoud Tahani**[1]

Received: 26 February 2025 / Revised: 23 May 2025 / Accepted: 22 June 2025

Abstract

Purpose This paper presents a novel bistable, multi-frequency hybrid energy harvesting mechanism with an adaptive potential barrier, aimed at improving energy scavenging efficiency in low-excitation environments.

Methods The system employs a recently developed bistable two-degree-of-freedom cut-out piezoelectric harvester, which achieves substantial power output through two closely positioned resonances. However, conventional bistable harvesters underperform when the excitation level is insufficient to overcome the potential barrier. To address this, an auxiliary magnetic oscillator is incorporated into the original cut-out harvester to lower the barrier dynamically and facilitate inter-well oscillations. Also, an induction coil surrounding the magnetic oscillator scavenges extra electrical power, further enhancing the overall power generation. The mathematical model is derived through a hybrid procedure combining the Ritz method with the Euler-Bernoulli beam and magnetic dipole theories. The model accuracy is validated by the available experimental observations for simpler systems. Furthermore, a bistability criterion is introduced, outlining the system properties required to trigger inter-well oscillations.

Results Numerical results demonstrate that the proposed harvester overcomes the potential barrier at lower excitation amplitudes and achieves higher generated power over a broader frequency bandwidth. Under a 4.5 m/s^2 excitation, the hybrid harvester generates a maximum average power of approximately 12 mW, representing a 118% improvement over the conventional design.

Conclusion The analyses confirm that the proposed hybrid design significantly improves energy harvesting efficiency compared to conventional designs reported in the literature.

Keywords Energy harvesting · Piezoelectric layers · Electromagnetic induction · Adaptive potential well · Bistability criterion

Introduction

Vibration-based energy harvesting has been the subject of numerous studies over the last decades due to its application in powering portable electronic devices and wireless sensors [1–3]. Currently, conventional chemical batteries serve as the main power source for these devices, suffering from limited life cycles, periodic replacement, and hazardous disposal. Hence, energy harvesting is a potential alternative to replace batteries or facilitate their regular recharging. The most common transduction technologies converting ambient kinetic energy into electricity are piezoelectric [4], electromagnetic [5], and electrostatic[6] mechanisms. Regardless of the transduction technique, traditional linear energy harvesters are designed based on the linear resonance concept. Thus, they reach the optimum performance when the excitation frequency matches the natural frequency of the system. This means the output power drops dramatically with a slight shift from the resonant frequency [7, 8]. Therefore, since ambient vibration sources are typically wideband and random, researchers have used a variety of strategies such as resonance tuning [9, 10], frequency-up conversion [11, 12], multi-mode structures [13, 14], and the introduction of nonlinearities [15, 16] to scavenge energy over a broader frequency range.

Among these, exploiting nonlinearities has shown promising results in broadening bandwidth and enhancing power output. Recent advances have extended nonlinear energy harvesting principles to more complex structures such

---

✉ Amir R. Askari
ar.askari@hsu.ac.ir; a.askari@hud.ac.uk

✉ Masoud Tahani
mtahani@um.ac.ir

[1] Department of Mechanical Engineering, Ferdowsi University of Mashhad, Mashhad, Iran

[2] Department of Mechanical Engineering, Hakim Sabzevari University, Sabzevar, Iran

[3] Department of Engineering and Technology, The University of Huddersfield, Huddersfield HD1 3DH, UK

as fluid-conveying pipes, where self-powered sensing and vibration suppression are critical. Tang et al. [17] investigated the effects of PEH coupled with nonlinear energy sinks (NES) in functionally graded pipes. They showed how three-directional material gradients and geometric nonlinearities improve energy conversion under complex boundary conditions. Gao et al. [18] demonstrated that incorporating mechanical stoppers into cantilevered fluid-conveying pipes introduces beneficial nonlinear stiffness characteristics, such as softening and hardening effects, that enhance energy harvesting efficiency.

A promising approach to widening the working frequency range of energy harvesters is to employ multi-mode techniques by integrating several oscillating units in one single device. Shahruz [19] and Xue et al. [20] proposed an array configuration of piezoelectric cantilever beams with different natural frequencies. Although this system can expand the operating frequency bandwidth, the harvester presents limited efficiency because only one of its components is active while the others are in an off-resonance state. Ou et al. [21] presented a double-mass piezoelectric cantilever beam to enhance the operating bandwidth of the harvester. Despite obtaining two useful modes, the two corresponding resonant frequencies were too far apart for the harvester to be considered broadband. Erturk et al. [22] investigated an L-shaped beam-mass configuration which can be tuned to have much closer the first two natural frequencies. To design a more applicable multi-mode energy harvester, the multiple resonance frequencies should be tuned to be close enough to each other. To this end, Kim et al. [23] introduced a two-degree-of-freedom (2-DoF) piezoelectric energy harvester (PEH) that utilized both translational and rotational displacements to achieve two close resonance peaks. Wu et al. [24] also proposed a 2-DoF PEH with a cut-out beam structure which can achieve two close resonances with significantly large voltage amplitudes. To scavenge energy from wideband, low frequency, and low amplitude vibration sources, Li et al. [25] introduced a multi-branch sandwich PEH. This harvester was composed of a substrate and multiple inner single branches, resulting in multiple close power peaks.

Another strategy to improve the harvester performance in terms of higher output power and broader bandwidth is exploiting nonlinearity through magnetic interactions. In particular, bistable energy harvesters (BEH) have been thoroughly studied due to their capability of broadband energy harvesting [26–29]. The main feature of bistable oscillators is the double-well potential curve, which comprises two potential wells (stable equilibrium points) separated by a potential barrier (unstable equilibrium point). BEHs can exhibit two distinct motions depending on the excitation intensity. For low levels of excitation, the harvester undergoes small-amplitude intrawell motions by oscillating about one of the stable equilibria. On the other hand, if the excitation reaches a certain threshold to overcome the potential barrier, the harvester exhibits large-amplitude inter-well oscillations between the two stable equilibria. Although a higher potential barrier may lead to increased output power due to the greater separation between potential wells, it simultaneously reduces the likelihood of triggering high-energy inter-well oscillations. Therefore, the performance of BEHs is highly dependent on the height of the potential barrier.

Various techniques have been proposed to facilitate the energetic inter-well oscillations by reducing the potential barrier's height while maintaining the distance between the potential wells. To this end, some researchers utilized mechanisms with fixed potential barriers including multi-stable (tri- or quad-stable) systems by adding additional fixed magnets to the conventional bistable harvester [30–32]. Zhou et al. [33] explored a magnetically coupled PEH with rotatable external magnets. Their results showed that the magnet inclination angle can sufficiently affect the operating bandwidth. To enhance the performance of a compressive-mode vibration energy harvester, Zou et al. [34] proposed a system that comprised a magnetic oscillator and a flextensional transducer attached to a magnet (magnetic stator). The two additional magnets were fixed on the flextensional transducers and symmetrically arranged on both sides of this magnetic stator. Their results showed that the magnetic force intervention allows the harvester to work effectively over a wide frequency range under low excitation levels. Alternatively, mechanisms that can adjust the potential barrier dynamically have been developed. Gao et al. [35] and Leng et al. [36] compared the bistable PEHs with the external magnets attached to the base using both fixed support and elastic support configurations. According to their numerical and experimental results, elastic support systems can outperform rigid support harvesters under low-intensity excitations owing to their variable potential function. Nguyen et al. [37] dynamically lowered the potential barrier of a bistable PEH by employing a mechanically rectified auxiliary magnetic oscillator to broaden the frequency range of the high-energy oscillations. Zhou et al. [38] proposed a flexible bistable harvester that comprised a piezoelectric cantilever beam with a tip magnet and a double-clamped beam with a mid-magnet. Due to the variability of the potential energy function of this system, the harvester can more easily undergo snap-through and generate a higher power output. Chen et al. [39] adopted a spring-magnetic oscillator to reduce the potential barrier of a bistable PEH. Their experimental and numerical results indicated that the proposed harvester could generate greater output power over a wider frequency range compared to the conventional BEH with a fixed potential barrier.

To further enhance the performance of the harvesters, researchers have combined nonlinear and multi-mode techniques to expand the operating bandwidth while maintaining high power output. Su et al. [8] designed a dual-cantilever PEH composed of outer and inner beams interacting by repulsive magnetic force. Their results demonstrated that this harvester can provide high output power over a broad frequency range. Wu et al. [40] incorporated magnetic interaction into a linear 2-DoF cut-out PEH. This provided them with a broader frequency bandwidth in mono-stable conditions. To increase the efficiency of harvesters operating on the basis of a bistable cut-out mechanism, Zayed et al. [41] introduced a quad-stable configuration by adding some extra magnets to the system. Their results indicated the supremacy of the quad-stable harvester over the BEH in terms of the wider operating frequency range and the higher voltage output. In the sequence of this work, Tian et al. [42] presented an inner-outer magnetic 2-DoF PEH by fixing another pair of magnets at the free end of the outer beam and base of the original nonlinear cut-out harvester. It was observed that the proposed harvester can provide a sufficiently broader frequency bandwidth in the lower frequency range. Furthermore, due to the introduction of the new magnetic force, the inner beam can more readily achieve inter-well oscillations under low excitation levels compared to the original nonlinear cut-out harvester. Despite these advancements, the aforementioned harvesters share a critical limitation: the potential barrier is fixed and cannot be dynamically adjusted. As a result, they may fail to trigger inter-well oscillations, especially under low-intensity excitations, thereby limiting their effectiveness in practical energy harvesting applications.

To address this limitation, this paper proposes a novel bistable multi-frequency hybrid energy harvester (MHEH) design, building upon the cut-out PEH originally developed by Wu et al. [40]. The proposed harvester integrates two key innovations: first, instead of using a fixed external magnet as in the traditional nonlinear cut-out harvester [40], an adaptive potential well is created by mounting the external magnet on a spring, thereby allowing it to oscillate. This approach dynamically lowers the potential barrier, facilitating inter-well motion even at low excitation levels. Second, the kinetic energy transferred to the auxiliary oscillator is converted into electrical power through an electromagnetic transduction mechanism. This mechanism works in tandem with the primary piezoelectric harvester, forming a hybrid system that significantly enhances energy conversion efficiency compared to the conventional design with a fixed magnet. Overall, these innovations enable the proposed MHEH to achieve higher energy conversion efficiency and a wider operational bandwidth than conventional systems. It is noteworthy that the novelties and main contributions of this research are summarized below:

- A PEH with a cut-out beam structure integrated with an electromagnetic transduction mechanism is proposed.
- Accounting for the distributed mass and stiffness of the structure, the coupled axial-transversal governing equations of motion are obtained through a hybrid procedure including the Ritz method.
- The influence of the magnetic excitation is taken into account based on the magnetic dipole theory, ensuring that the developed mathematical model closely reflects physical reality.
- Bifurcation and potential energy analyses are performed to identify combinations of system parameters that trigger high-energy inter-well oscillations. The resulting bistability criterion provides practical guidance for selecting appropriate parameters, serving as a valuable tool for engineers involved in the design of energy harvesters.
- The adaptive potential barrier of the proposed harvester enables the activation of inter-well oscillations under lower excitation intensities. Furthermore, the harvester demonstrates enhanced power output across a broader frequency range, with a maximum average power of 12 mW, representing a 118% improvement over conventional cut-out harvesters.

The rest of the paper is organized as follows. In Sect."System Structure and Modeling", the mathematical model of the proposed harvester is established based on the Euler–Bernoulli beam and magnetic dipole theories. The nonlinear equations of motion associated with the system are then derived employing Hamilton's principle along with a hybrid procedure including the Ritz method. Sect."Results and Discussions"presents a comprehensive analysis of the harvester's performance. First, the accuracy of the proposed mathematical model is validated using experimental results from the literature, corresponding to a system with a simpler design. Second, potential and bifurcation analyses are conducted to establish a bistability criterion that guides the selection of system parameters for inducing inter-well oscillations. Furthermore, the superiority of the proposed system over the conventional harvester is demonstrated, and the influence of magnetic oscillator parameters and resistive loads on system performance is investigated. Finally, conclusions are briefly presented in Sect."Conclusions".

System Structure and Modeling

Harvester Structure and Description

A schematic of the nonlinear multi-frequency hybrid harvester proposed in this paper is shown in Fig. 1. The harvester comprises a cut-out beam and a spring-loaded permanent magnet that is attached to the base. The cut-out structure consists of cantilever outer beams attached to an

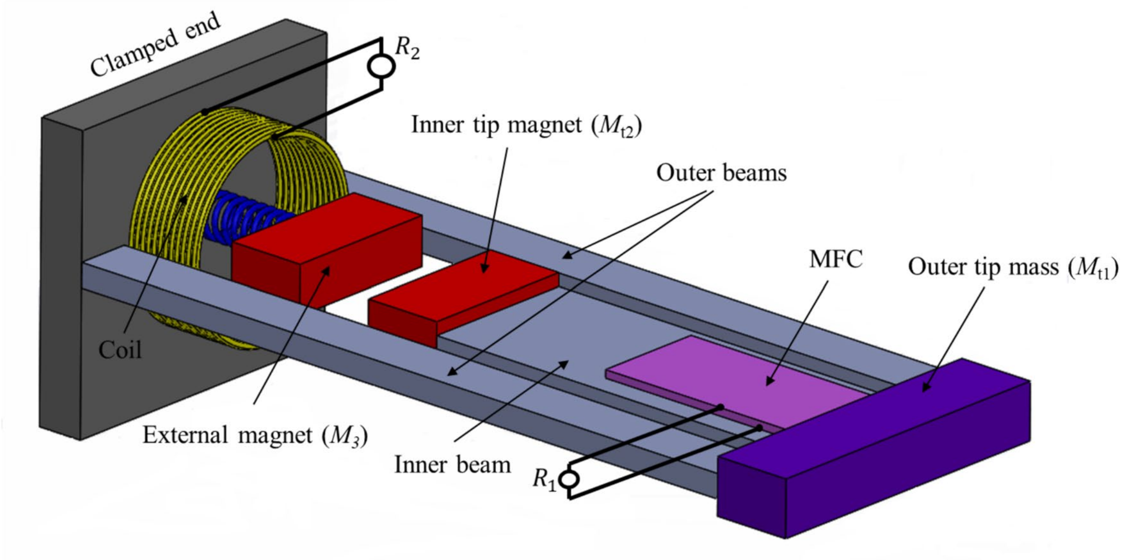

Fig. 1 Schematic of the proposed hybrid harvester

outer tip mass (M_{t1}). An inner cantilever beam, partially covered by a Macro Fiber Composite (MFC) piezoelectric transducer in a unimorph configuration, is also attached to a permanent magnet as an inner tip mass (M_{t2}). The magnetic oscillator is axially aligned with the inner beam axis and an induction coil is fixed around it. The polarities of magnets are in opposite directions to induce a repulsive force. The initial distance between them is d_0.

When the base is excited, the outer and inner beams vibrate. As a result, the bending of the inner beam produces a voltage in the piezoelectric layer. On the other hand, the repulsive force between the magnetic masses causes the external magnet to oscillate inside the induction coil, in response to the inner beam vibrations. Therefore, the oscillation of the external magnet induces a current in the surrounding coil according to Faraday's law of induction.

In order to mathematically model the proposed harvester, the system is segmented into three sections, including the outer beams, inner beam, and magnetic oscillator. These sections and their corresponding local coordinates are depicted in Fig. 2. As can be seen from Fig. 2a, L1, L2, and L_p represent the lengths of the outer substrate, inner substrate, and piezoelectric layer, respectively. According to the previous studies, the transverse displacements of the outer and inner beams are in opposite directions for the first two vibration modes [40]. Thus, the positive directions of the transverse coordinates are regarded as being opposite to each other, as illustrated in Fig. 2b.

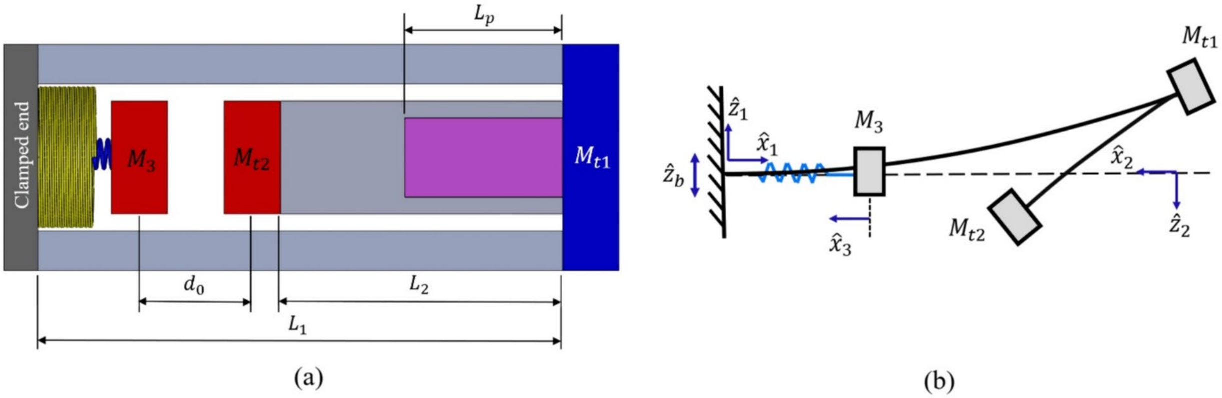

Fig. 2 **a** Top view of the proposed harvester and **b** local coordinates attached to each part of the harvester

Mathematical Modeling

Employing the Euler–Bernoulli beam theory, the displacement field associated with each part of the cut-out beam is given by

$$\begin{aligned} &u_i = \hat{u}_i - \hat{z}_i \tfrac{\partial \hat{w}_i}{\partial \hat{x}_i}, \\ &v_i = 0, \qquad \text{for } 0 < \hat{x}_i < L_i \qquad i = 1,2 \\ &w_i = \hat{w}_i \end{aligned} \tag{1}$$

where the indices $i = 1$ and 2 denote the outer and inner beams, respectively. Furthermore, $\hat{u}$ and $\hat{w}$ represent the axial and transverse displacements of a point located on the mid-surface of the beam along the $\hat{x}$ and $\hat{z}$ axes, respectively. Also, the displacement of the magnetic oscillator is represented by $\hat{u}_3$. It is worth mentioning that the harvester is subjected to the harmonic base displacement of the form $\hat{z}_b = \hat{Z}\cos(\omega\hat{t})$ with $\hat{Z}$ and ω representing the excitation amplitude and frequency.

Given the displacement field in Eq. (1), the only non-zero component of the strain tensor is as follows

$$\varepsilon_x{}^{(i)} = \frac{\partial u_i}{\partial x} = \frac{\partial \hat{u}_i}{\partial \hat{x}_i} - \hat{z}_i \frac{\partial^2 \hat{w}_i}{\partial \hat{x}_i^2}, i = 1,2. \tag{2}$$

The axial stress induced in the substrates is expressed as $\sigma_x^{(i)} = E_s \varepsilon_x{}^{(i)}$, where E_s denotes Young's modulus of the substrates. The constitutive equations that relate the mechanical stress (σ_p) and electrical displacement (D_z) of the piezoelectric material to its strain and electric field (E_z) can be written as

$$\begin{aligned} \sigma_p &= E_p \varepsilon_x{}^{(2)} - e_{31} E_z, \\ D_z &= e_{31} \varepsilon_x{}^{(2)} + \varepsilon_{33} E_z, \end{aligned} \tag{3}$$

where E_p is the elastic modulus of the piezoelectric layer, and e_{31} and ε_{33} represent its coupling coefficient and dielectric constant, respectively. The electric field can be expressed as a function of the voltage induced in the piezoelectric layer as $E_z = V/h_p$ with h_p denoting the piezoelectric thickness [43].

The total potential energy of the proposed harvester is given by [44]

$$U = \sum_{i=1}^{2} \left(\frac{1}{2} \int_0^{L_i} \left[N_x^{(i)} \frac{\partial \hat{u}_i}{\partial \hat{x}_i} - M_x^{(i)} \frac{\partial^2 \hat{w}_i}{\partial \hat{x}_i^2} \right] \mathrm{d}\hat{x}_i \right) + \frac{1}{2} K_3 \hat{u}_3^2 + \frac{1}{2} L_c \dot{Q}_2^2 + U_e + U_m, \tag{4}$$

where K_3 is the stiffness of the magnetic oscillator and L_c and Q_2 are the inductance and the charge passing through the coil, respectively. Also,U_e is the electrical energy stored in the piezoelectric layer and U_m represents the magnetic potential energy which will be calculated later in this paper. Furthermore, $N_x^{(i)}$ and $M_x^{(i)}$ denote the stress resultants which are given by [45]

$$\begin{aligned} N_x^{(i)} &= \int_{A_{si}} \sigma_x^{(i)} dA_{si} + (i-1) \int_{A_p} \sigma_p dA_p H\left(L_p - \hat{x}_i\right), \\ M_x^{(i)} &= \int_{A_{si}} \sigma_x^{(i)} . \hat{z}_i dA_{si} + (i-1) \int_{A_p} \sigma_p . \hat{z}_i dA_p H\left(L_p - \hat{x}_i\right), \end{aligned} \tag{5}$$

where A_s and A_p represent the cross-sectional areas of the substructures and piezoelectric layer, respectively. Also, H stands for the Heaviside function.

The internal electrical energy stored in the piezoelectric layer, which appeared in Eq. (4), is as follows [43]

$$\begin{aligned} U_e &= \tfrac{1}{2} \int_0^{L_2} \int_{A_p} D_z E_z H\left(L_p - \hat{x}_2\right) dA_p d\hat{x}_2 \\ &= -\frac{\hat{V}}{2h_p} \int_0^{L_2} \left[A_e \frac{\partial \hat{u}_2}{\partial \hat{x}_2} - B_e \frac{\partial^2 \hat{w}_2}{\partial \hat{x}_2^2} \right] H\left(L_p - \hat{x}_2\right) d\hat{x}_2 + \frac{\varepsilon_{33} L_p A_p \hat{V}^2}{2{h_p}^2}, \end{aligned} \tag{6}$$

where [45]

$$A_e = \int_{A_p} e_{31} dA_p, B_e = \int_{A_p} e_{31} . \hat{z}_2 dA_p. \tag{7}$$

The total kinetic energy of the harvester is the sum of the kinetic energies of the cut-out beam and the magnetic oscillator which is expressed as [43]

$$\begin{aligned} T = \textstyle\sum_{i=1}^{2} \Bigg\{ & \tfrac{1}{2} \int_0^{L_i} \Bigg[I_0^{(i)} \left(\left(\tfrac{\partial \hat{u}_i}{\partial \hat{t}} \right)^2 + \left(\tfrac{\partial \left(\hat{w}_i + (-1)^{i+1} \hat{z}_b \right)}{\partial \hat{t}} \right)^2 \right) - 2 I_1^{(i)} \tfrac{\partial \hat{u}_i}{\partial \hat{t}} \tfrac{\partial^2 \hat{w}_i}{\partial \hat{x}_i \partial \hat{t}} \\ & + I_2^{(i)} \left(\tfrac{\partial^2 \hat{w}_i}{\partial \hat{x}_i \partial \hat{t}} \right)^2 \Bigg] \mathrm{d}\hat{x}_i + \tfrac{1}{2} M_{ti} \left(\left(\tfrac{\partial \hat{u}_i}{\partial \hat{t}} \right)^2 + \left(\tfrac{\partial \left(\hat{w}_i + (-1)^{i+1} \hat{z}_b \right)}{\partial \hat{t}} \right)^2 \right) \Bigg|_{\hat{x}_i = L_i} \\ & + \tfrac{1}{2} I_{ti} \left(\tfrac{\partial^2 \hat{w}_i}{\partial \hat{x}_i \partial \hat{t}} \right)^2 \Bigg|_{\hat{x}_i = L_i} \Bigg\} + \tfrac{1}{2} M_3 \left(\tfrac{\partial \hat{u}_3}{\partial \hat{t}} \right)^2, \end{aligned} \tag{8}$$

where I_{ti} is the mass moment of inertia associated with the outer and inner tip masses and M_3 denotes the mass of the external magnet. Also, the zeroth, first, and second moments of the cross-sectional area are as follows [43]

$$\begin{aligned} I_0^{(i)} &= \int_{A_{si}} \rho_{si} dA_{si} + (i-1) \int_{A_p} \rho_p dA_p H\left(L_p - \hat{x}_i\right), \\ I_1^{(i)} &= \int_{A_{si}} \rho_{si} . \hat{z}_i dA_{si} + (i-1) \int_{A_p} \rho_p . \hat{z}_i dA_p H\left(L_p - \hat{x}_i\right), \\ I_2^{(i)} &= \int_{A_{si}} \rho_{si} . \hat{z}_i^2 dA_{si} + (i-1) \int_{A_p} \rho_p . \hat{z}_i^2 dA_p H\left(L_p - \hat{x}_i\right). \end{aligned} \tag{9}$$

Due to the slenderness of the beam, the rotational kinetic energy can be neglected compared to that associated with the translational motion [46]. Thus, the kinetic energy contributions from the rotary inertias of $I_1^{(i)}$ and $I_2^{(i)}$ can be ignored.

The virtual work done by the non-conservative forces can be written as [44]

$$\delta W_{nc} = -2\int_0^{L_1} c_1 \frac{\partial \widehat{w}_1}{\partial \widehat{t}} \delta \widehat{w}_1 d\widehat{x}_1 - \int_0^{L_2} c_2 \frac{\partial \widehat{w}_2}{\partial \widehat{t}} \delta \widehat{w}_2 d\widehat{x}_2 - c_3 \frac{\partial \widehat{u}_3}{\partial \widehat{t}} \delta \widehat{u}_3$$
$$-F_e \delta \widehat{u}_3 - Q_1 \delta \widehat{V} - \left(R_c + R_2\right)\dot{Q}_2 \delta Q_2 + \varepsilon \delta Q_2, \tag{10}$$

where $c_i (i = 1 - 3)$ denotes the viscous damping ratio associated with the outer beams, inner beam, and magnetic oscillator, respectively. Q_1 is the electrical charge corresponding to the piezoelectric layer. R_2 and R_c represent the resistance of the electromagnetic circuit and the internal resistance of the induction coil, respectively. Also, ε and F_e denote the electromotive and backward coupling forces which are discussed in the next section.

Electromagnetic Coupling Coefficient and Magnetic Force

The geometrical configuration of the tip magnet and the moving external magnet is depicted in Fig. 3. Herein, the permanent magnets are modeled as magnetic dipoles [26] with the magnetic moment vectors $\boldsymbol{m}_A$ and $\boldsymbol{m}_B$ as below

$$\boldsymbol{m}_A = MV\cos\theta\,\widehat{\boldsymbol{e}}_x - MV\sin\theta\,\widehat{\boldsymbol{e}}_z, \qquad \boldsymbol{m}_B = -MV\widehat{\boldsymbol{e}}_x, \tag{11}$$

where V and M are the volume and magnetization of the magnet, respectively. The magnetization is related to the residual magnetic flux B_r as $M = \frac{B_r}{\mu_0}$, where $\mu_0 = 4\pi \times 10^{-7}$ H/m is the permeability of the vacuum [32]. Also, θ is the rotation angle of the tip magnet, which can be expressed as $\theta = \arctan\left[w_2{\prime}\left(L_2, t\right)\right]$, where the prime sign denotes the first derivative with respect to $\widehat{x}_2$.

In view of Fig. 3, the displacement vector connecting the center of magnet B to that of the magnet A is given by

$$\boldsymbol{r}_{BA} = \left(-d_0 - \widehat{u}_3\right)\widehat{\boldsymbol{e}}_x - \widehat{w}_{t2}\widehat{\boldsymbol{e}}_z, \tag{12}$$

where d_0 denotes the initial gap between the magnets and w_{t2} is the tip displacement of the inner beam. It is noteworthy that the contribution of the axial displacement related to the tip of the inner beam in Eq. (12) is ignored since it is very small compared to the displacement of the external magnet.

According to the magnetic dipole principle, the magnetic field generated by the tip magnet (i.e., magnet A) on the external magnet (i.e., magnet B) is expressed as [26]

$$\boldsymbol{B}_{AB} = -\frac{\mu_0}{4\pi}\nabla\frac{\boldsymbol{m}_A.\boldsymbol{r}_{BA}}{\left|\boldsymbol{r}_{BA}\right|^3}, \tag{13}$$

where ∇ is the vector differential operator.

From Eq. (13), the general form of the magnetic potential energy can be expressed as [32]

$$U_m = -\boldsymbol{m}_B.\boldsymbol{B}_{AB}. \tag{14}$$

Upon substituting Eqs. (11-13) into Eq. (14), the final form of the magnetic potential energy is given by

$$U_m = \frac{\mu_0 M^2 V^2}{4\pi}\left[\frac{3\left(-d_0-\widehat{u}_3\right)^2 cos\,\theta - 3\left(-d_0-\widehat{u}_3\right)\widehat{w}_{t2} sin\,\theta}{\left|\boldsymbol{r}_{BA}\right|^5} - \frac{cos\,\theta}{\left|\boldsymbol{r}_{BA}\right|^3}\right]. \tag{15}$$

It is worth mentioning that the magnetic force components along the x and z directions can, respectively, be written as [47]

$$F_x = -\frac{\partial U_m}{\partial \widehat{u}_3}, F_z = -\frac{\partial U_m}{\partial \widehat{w}_{t2}}. \tag{16}$$

As Fig. 4 shows, the external magnet moves inside the induction coil along its central axis. All electromagnetic converters work based on Faraday's law of induction. According to this law, the relative motion between the magnet and the coil generates a voltage between the coil terminals. This induced

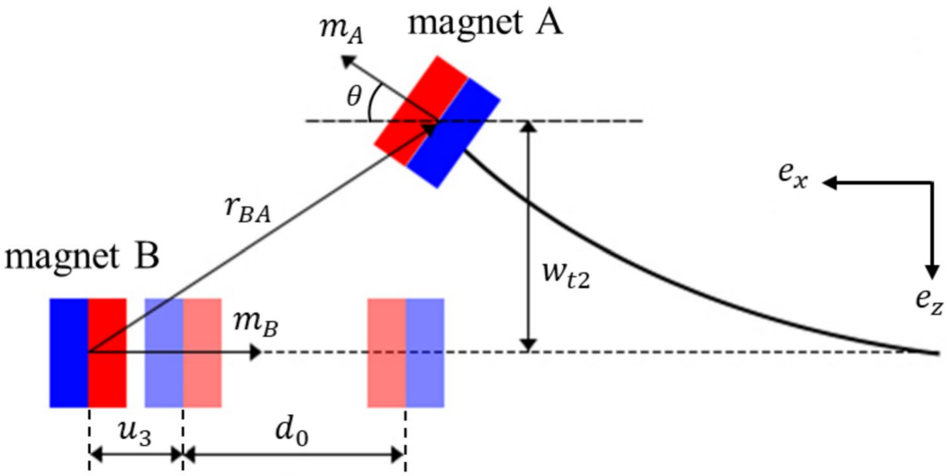

Fig. 3 Magnetic moment vectors and displacements of the magnetic masses of the harvester

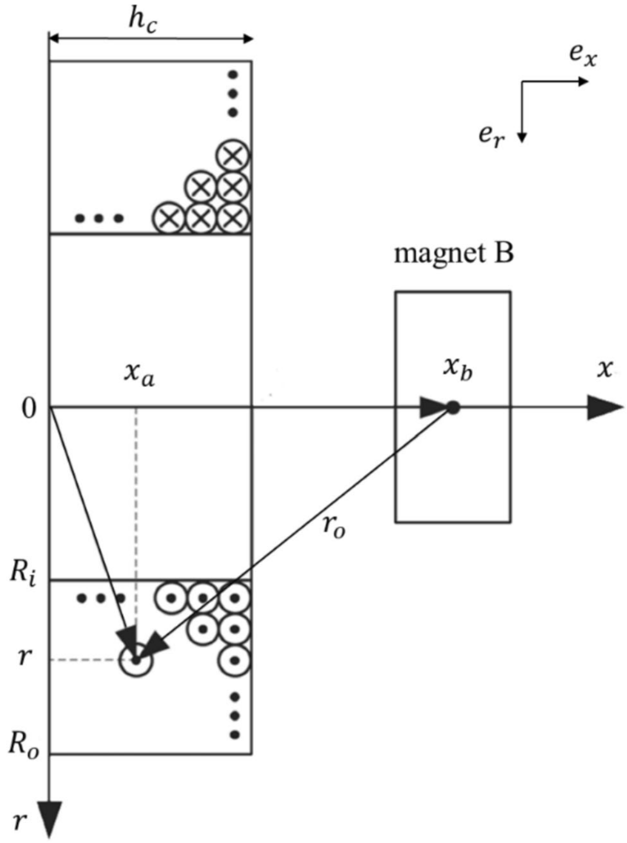

Fig. 4 The relative position between the external magnet and the coil

voltage ε is proportional to the rate of change of the magnetic flux Φ_B as below [48]

$$\varepsilon = -\frac{d\Phi_B}{dt} = -\frac{d\Phi_B}{dx} \bullet \frac{dx}{dt} = \theta_{em}\dot{x}, \tag{17}$$

where θ_{em} represents the electromagnetic coupling coefficient which will be calculated later in this section.

Connecting the coil terminals to a load resistance allows a current to flow in the coil. This current creates an opposing magnetic field which results in a backward coupling force as expressed below [49]

$$F_e = \theta_{em}\dot{Q}_2. \tag{18}$$

The magnetic field generated by the moving external magnet (magnet B) at any location (for instance at an arbitrary wire of the induction coil) can be expressed as [50]

$$\boldsymbol{B} = -\frac{\mu_0}{4\pi}\left[\frac{\boldsymbol{m}_B}{\left|\boldsymbol{r}_0\right|^3} - \frac{3\boldsymbol{r}_0\left(\boldsymbol{m}_B \cdot \boldsymbol{r}_0\right)}{\left|\boldsymbol{r}_0\right|^5}\right], \tag{19}$$

where $\boldsymbol{r}_0 = \left(x_a - x_b\right)\hat{\boldsymbol{e}}_x + r\hat{\boldsymbol{e}}_r$ denotes the displacement vector from an arbitrary wire to the magnet core, as depicted in Fig. 5.

It is seen from Eq. (17) that the induced voltage is related to the magnetic flux gradient along the x-axis. Thus, considering only the normal component of the magnetic field along a line passing through the magnet center, the magnetic flux over the area enclosed by a wire is expressed as [51]

$$\Phi = \oint_s B_x dA = \frac{B_r V r^2}{2\left[r^2 + \left(x_a - x_b\right)^2\right]^{3/2}}. \tag{20}$$

Thus, the total magnetic flux through the N-turn coil can be given by [50]

$$\Phi_B = \frac{f_c N}{A_c}\int_0^{h_c}\int_{R_i}^{R_o} \Phi dr dx_a, \tag{21}$$

where $A_c = \left(R_o - R_i\right)h_c$ is the cross-sectional area and $f_c = \frac{NA_w}{A_c}$ is the filling factor of the coil. Also, R_i, R_o, and h_c are the inner radius, outer radius, and height of the induction coil. Furthermore, A_w is the cross-sectional area of a single wire.

Upon substitution of Eq. (21) into Eq. (17), the electromagnetic coupling coefficient θ_{em} can be calculated as [50]

$$\begin{aligned}\theta_{em} = -\frac{f_c N}{2A_c}\Bigg[&\ln\frac{R_i+\sqrt{R_i{}^2+\left(x_b-h_c\right)^2}}{R_o+\sqrt{R_o{}^2+\left(x_b-h_c\right)^2}} + \ln\frac{R_o+\sqrt{R_o{}^2+x_b{}^2}}{R_i+\sqrt{R_i{}^2+x_b{}^2}} \\ &+\frac{R_o}{\sqrt{R_o{}^2+\left(x_b-h_c\right)^2}} - \frac{R_o}{\sqrt{R_o{}^2+x_b{}^2}} - \frac{R_i}{\sqrt{R_i{}^2+\left(x_b-h_c\right)^2}} \\ &+\frac{R_i}{\sqrt{R_i{}^2+x_b{}^2}}\Bigg]\end{aligned} \tag{22}$$

Coupled Electromechanical Equations

To derive the equations of motion associated with the present multi-mode hybrid harvester, Hamilton's principle is utilized. This principle states [43]

$$\int_{t_1}^{t_2}\left(\delta U - \delta T - \delta W_{nc}\right)d\hat{t} = 0, \tag{23}$$

where δU and δT denote the variation of the potential and kinetic energies, respectively.

Taking into consideration that the axial kinetic energy of the beam can be neglected in comparison with that of the transverse motion for a slender beam [45], the axial resultant force corresponding to each of the outer and inner beams $N_x^{(i)}$ remains constant along the beam's length. Therefore, the axial resultant force is equal to its average along the length of the beam. Hence, one can write

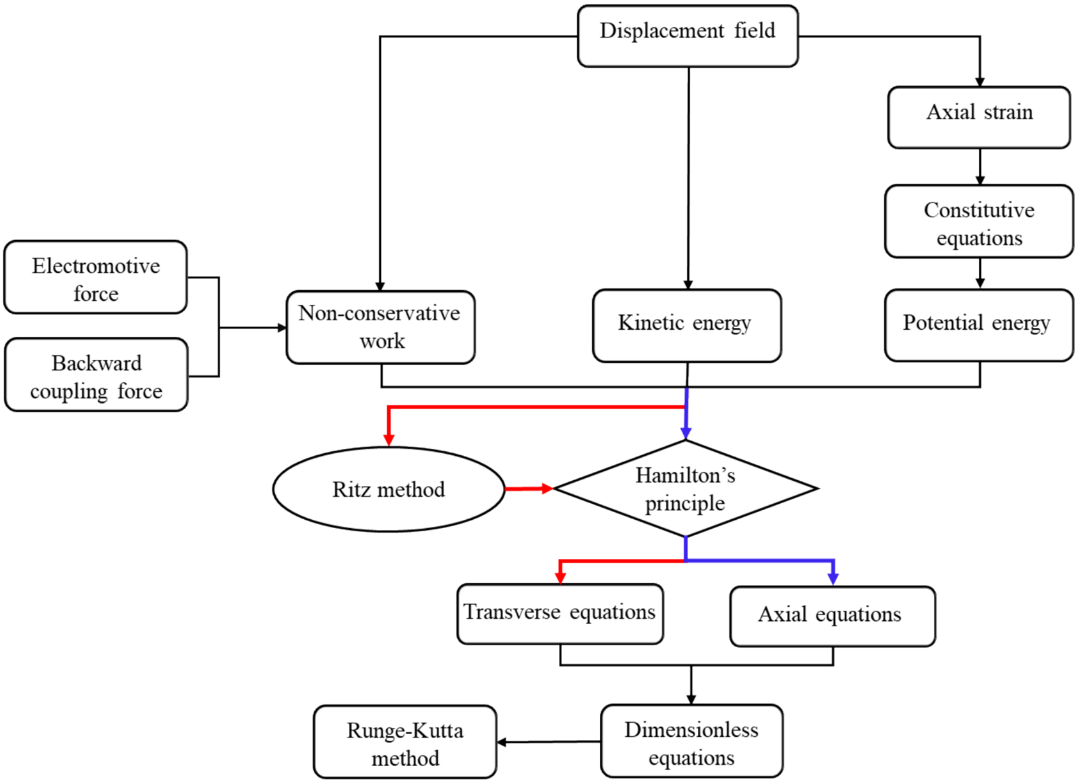

Fig. 5 Modeling procedure associated with the proposed hybrid harvester

$$\overline{N}_x^{(i)} = \frac{1}{L_i}\int_0^{L_i} N_x^{(i)} dx_i. \tag{24}$$

Herein, the coupled electromechanical equations of the harvester can be obtained using a hybrid method. That is, first, the axial equations of motion corresponding to the cut-out beam, and the coupled equations of the magnetic oscillator are derived by adopting Hamilton's principle along with the fundamental lemma of the calculus of variations as below

$$\begin{aligned} &\overline{N}_x^{(1)} + M_{t1}\frac{\partial^2 \hat{u}_{t1}}{\partial \hat{t}^2} = 0, \\ &\overline{N}_x^{(2)} + M_{t2}\frac{\partial^2 \hat{u}_{t2}}{\partial \hat{t}^2} + F_x = 0, \\ &M_3\ddot{\hat{u}}_3 + c_3\dot{\hat{u}}_3 + K_3\hat{u}_3 + \theta\hat{I} - F_x = 0, \\ &L_c\dot{\hat{I}} + \left(R_c + R_2\right)\hat{I} - \theta\dot{\hat{u}}_3 = 0, \end{aligned} \tag{25}$$

where u_{t1} and u_{t2} stand for the axial displacements of the tips of the outer and inner beams, respectively. Also, the overdot symbol indicates the time derivative.

Having the axial equations of motion of the harvester, the transverse equations of the proposed MHEH can then be obtained employing the Ritz method for discretization, which states that the transverse displacement of the beam can be expressed in terms of the generalized coordinates. Thus, the transverse displacement of each section of the cut-out beam can be expressed as

$$\hat{w}_i\left(\hat{x}_i, \hat{t}\right) = \sum_{r=1}^{\infty} \varphi_{ir}\eta_r i = 1{,}2, \tag{26}$$

where φ_{ir} is the mode-shape of each section of the beam which can be set to satisfy essential boundary conditions and is given in Appendix A. η_r is the generalized coordinate of the r^{th} vibration mode.

For convenience, the following dimensionless parameters are introduced

$$\begin{aligned} &x_1 = \frac{\hat{x}_1}{L_1}, x_2 = \frac{\hat{x}_2}{L_2}, t = \frac{\hat{t}}{T}, u_1 = \frac{\hat{u}_1}{L_1}, u_2 = \frac{\hat{u}_2}{L_2}, u_3 = \frac{\hat{u}_3}{L_1}, w_1 = \frac{\hat{w}_1}{L_1}, w_2 = \frac{\hat{w}_2}{L_1}, \\ &z_b = \frac{\hat{z}_b}{L_1}, \Omega = \omega T, V = \frac{\hat{V}}{V^*}, I = \frac{\hat{I}}{I^*}, T = \sqrt{2\rho_s A_{s1} L_1^2}, V^* = \frac{B_e h_p L_1}{\varepsilon_{33} A_p L_p L_2}, I^* = \frac{L_1}{L_c} \end{aligned} \tag{27}$$

By substituting Eq. (26) into Eq. (23) and employing the fundamental lemma of calculus of variations, the governing normalized equations of the proposed nonlinear harvester in terms of the displacements can be obtained as follows

$$
\begin{aligned}
&\ddot{u}_{t1} + f_1 u_{t1} = 0,\\
&\ddot{u}_{t2} + g_1 u_{t2} + g_2 \eta_1 + g_3 \eta_2 + g_4 V + g_5 F_x = 0,\\
&\ddot{u}_3 + h_1 \dot{u}_3 + h_2 u_3 + h_3 I + h_4 F_x = 0,\\
&\ddot{\eta}_1 + p_1 \ddot{\eta}_2 + p_2 \dot{\eta}_1 + p_3 \dot{\eta}_2 + p_4 \eta_1 + p_5 \eta_2 + p_6 u_{t2} + p_7 V + p_8 F_z\\
&\ +p_9 Zcos(\Omega t) = 0,\\
&\ddot{\eta}_1 + q_1 \ddot{\eta}_2 + q_2 \dot{\eta}_1 + q_3 \dot{\eta}_2 + q_4 \eta_1 + q_5 \eta_2 + q_6 u_{t2} + q_7 V + q_8 F_z\\
&\ +q_9 Zcos(\Omega t) = 0,\\
&\dot{V} + r_1 \dot{u}_{t2} + r_2 \dot{\eta}_1 + r_3 \dot{\eta}_2 + r_4 V = 0\\
&\dot{I} + s_1 \dot{u}_3 + s_2 I = 0,
\end{aligned}
\tag{28}
$$

where Z stands for the normalized base acceleration and is given by $Z = \frac{\hat{Z}T^2}{L_1}$. Also, Ω represents the normalized excitation frequency. The coefficients f_1, $g_i(i = 1-5)$, $h_i(i = 1-4)$, $p_i(i = 1-8)$, $q_i(i = 1-7)$, $r_i(i = 1-4)$, and $s_i(i = 1,2)$ are given in Appendix B.

The process of deriving the mathematical model of the present hybrid harvester is summarized in the flowchart depicted in Fig. 5. To model the system, the Euler–Bernoulli displacement field is utilized to obtain the corresponding axial strains. Next, the constitutive equations associated with the proposed system are employed to derive the potential energy of the harvester. Following this, the kinetic energy and the work done by non-conservative forces are calculated based on the introduced displacement field. Finally, substituting these energy expressions into Hamilton's principle and integrating the outputs by parts just for the axial directions, the axial governing equations are derived. Neglecting the axial inertia of the beams in comparison to those of the tip masses, and discretizing the transverse deflections according to the Ritz method, the transverse equations of motion are also obtained. Ultimately, the equations of motion will be solved using the Runge–Kutta method.

The average output power generated within the piezoelectric and electromagnetic circuits are, respectively, given by

$$
P_p = \frac{1}{T}\int_0^T \frac{V^2}{R_1} dt, P_e = \frac{1}{T}\int_0^T I^2 R_2 dt,
\tag{29}
$$

where T is a sufficiently large time period compared to the period of the base excitation (i.e., ${}^{2\pi}/_{\omega}$). Also, R_1 represents the resistance of the piezoelectric circuit. The total average power generated by the harvester is the sum of the power generated by the piezoelectric layer and induction coil

$$
P = P_p + P_e.
\tag{30}
$$

Results and Discussions

Validation of the Mathematical Model

The accuracy of the proposed mathematical model is validated through comparison with experimental data from the literature, specifically the nonlinear cut-out beam with a fixed external magnet, as reported by Zayed et al. [41]. In this setup, the inner beam is covered by a piezoelectric layer (K2512U1, KINEZ) and the system is subjected to the base acceleration with an amplitude of 3 m/s^2. The outer tip mass, inner tip mass, and gap distance are set to 23.8 gr, 7.6 gr, and 23.5 mm, respectively. The other geometrical and physical properties of the harvester are presented in Table 1. It is to be noted that, unless stated otherwise, these properties are consistently applied throughout the study.

To validate the proposed mathematical approach, the reduced equations of motion in (28) are solved numerically using the MATLAB command ode45. Figure 6 compares the root mean square (RMS) values of the piezoelectric voltage predicted by the numerical solution with the experimental observations reported by Zayed et al. [41]. As is seen from this figure, the results from the proposed model are in close agreement with those observed experimentally. This consistency demonstrates the reliability of the proposed approach in predicting the behavior of similar energy harvesting systems, such as the one under investigation in this study.

Potential Energy Surface

As mentioned earlier, the magnetic oscillator is employed to adjust the harvester's potential barrier dynamically. Therefore, it is essential to investigate the impact of the newly introduced moving magnet on the system's potential energy function. In this study, the piezoelectric layer is assumed to be sufficiently thin such that its effect on the onset of bistable motion is negligible [52]. Furthermore, while damping effects—such as those arising from the electromagnetic coil—can influence the system's dynamic behavior and the stability of equilibrium points, they do not alter the existence or position of these points as determined by the potential energy [53]. Therefore, based on the theoretical framework established in Sect."System Structure and Modeling", the total potential energy expression for the proposed nonlinear multi-mode energy harvester, excluding the effects of both the piezoelectric layer and the induction coil, is reformulated as below

$$
U_t = \frac{1}{2}K_1{\eta_1}^2 + \frac{1}{2}K_2{\eta_2}^2 + \frac{1}{2}K_3\hat{u}_3^2 + U_m\left(u_3, \eta_1, \eta_2\right),
\tag{31}
$$

where K_1, K_2, and K_3 are the linear stiffnesses of the outer beams, inner beam, and spring, respectively. η_1 and η_2 are the generalized coordinates corresponding to the first and

Table 1 Geometric dimensions and material properties of the proposed hybrid harvester

Parameter	Symbol	Value
Piezoelectric transducer		
Each outer substrate length × width × thickness (mm^3)	$L_1 \times b_{s1} \times h_{s1}$	$93 \times 7 \times 0.5$
Inner substrate length × width × thickness (mm^3)	$L_2 \times b_{s2} \times h_{s2}$	$50 \times 20 \times 0.2$
Substrate density (kg/m^3)	ρ_s	7500
Substrate Young's modulus (GPa)	E_s	210
MFC layer length × width × thickness (mm^3)	$L_p \times b_p \times h_p$	$28 \times 14 \times 0.25$
MFC density (kg/m^3)	ρ_p	5440
MFC Young's modulus (GPa)	E_p	30.336
Piezoelectric constants (C/m^2)	e_{31}	−5.16
Dielectric permittivity (nF)	ε_{33}	12.653
Outer and inner tip masses (gr)	M_{t1}, M_{t2}	10.4, 17.33
Electromagnetic transducer		
External mass (gr)	M_3	30
Spring stiffness (N/m)	K_3	200
Magnet radius × height (mm^2)	$\mathrm{R} \times h_m$	6×10
Residual magnetic flux density (T)	B_r	1.1
Coil inner radius × outer radius × height (mm^3)	$R_i \times R_o \times h_c$	$10 \times 13 \times 17$
Coil turns	N	3500
Wire diameter (mm)	d_w	0.12
Wire resistance per unit length (Ω/ m)	ρ_c	1.511

second modes of the cut-out beam. According to Eq. (26), these coordinates are related to the transverse displacements of the outer beam tip (i.e., $\widehat{w}_{t1}$) and the inner beam tip (i.e., $\widehat{w}_{t2}$) through the following linear relations

$$\begin{aligned} \widehat{w}_{t1} &= \varphi_{11}(L_1)\eta_1 + \varphi_{12}(L_1)\eta_2, \\ \widehat{w}_{t2} &= \varphi_{21}(L_2)\eta_1 + \varphi_{22}(L_2)\eta_2 \end{aligned} \tag{32}$$

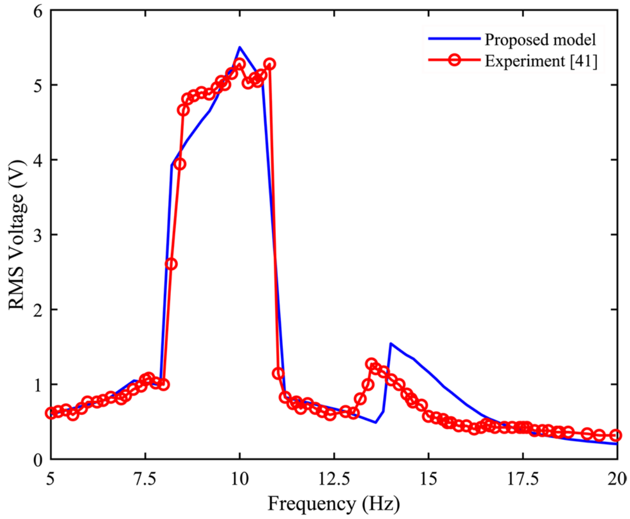

Fig. 6 Comparison of the voltage frequency response obtained by the proposed mathematical model and experimental results [41] for a bistable cut-out PEH with a fixed magnet

By solving Eq. (32) for η_1 and η_2 and substituting these expressions into Eq. (31), the total potential energy is reformulated as a function of $\widehat{w}_{t1}$, $\widehat{w}_{t2}$, and $\widehat{u}_3$. Since the magnetic force is applied only to the inner tip mass and the external magnet, the bistable behavior of the system is primarily determined by the interaction between their respective displacements, $\widehat{w}_{t2}$ and $\widehat{u}_3$. To isolate the effects of this coupling, $\widehat{w}_{t1}$ is kept constant. The potential energy surface of the multi-frequency harvester is then generated by varying $\widehat{w}_{t2}$ and $\widehat{u}_3$ over a defined grid, as shown in Fig. 7a. The black-colored trajectory on the three-dimensional surface is the potential energy of the proposed harvester obtained by quasi-statically changing $\widehat{w}_{t2}$ for a full cycle of motion and solving the static form of the governing equations for $\widehat{u}_3$. All system parameters are as listed in Table 1, with the initial gap between the magnets set to 23 mm.

In the proposed harvester, the external magnet oscillates in response to the inner beam oscillations. As the tip magnet approaches the center position (i.e., $\widehat{w}_{t2} = 0$), the repulsive magnetic force pushes the external magnet away from its equilibrium position (i.e., $\widehat{u}_3 = u_0$), where the magnetic and elastic restoring forces are balanced. This interaction leads to a reduction in the potential energy barrier, as illustrated in the associated potential trajectory. With a lower barrier, the system requires less energy to transition between the potential wells, thereby increasing the likelihood of interwell oscillations [39]. Conversely, as the tip magnet leaves the center position, the external magnet moves back to its equilibrium state. During this motion, the potential energy

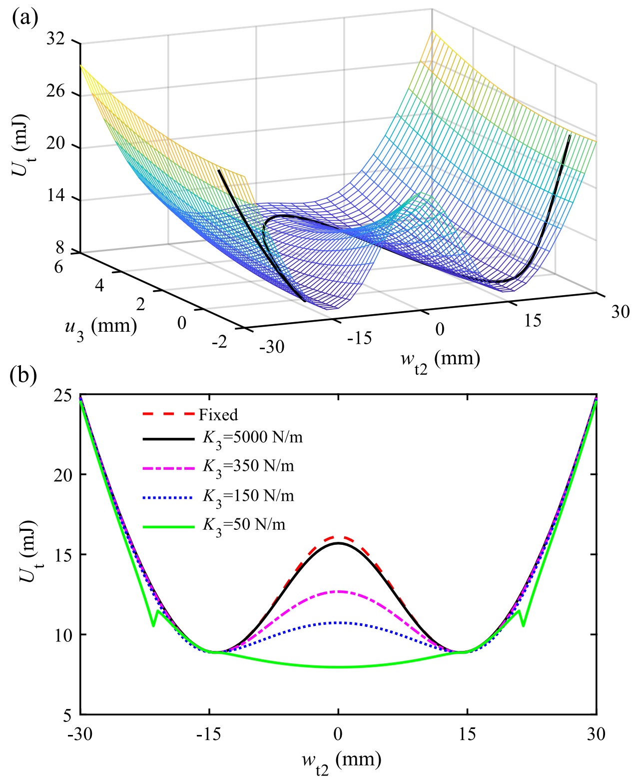

Fig. 7 **a** Potential energy surface of the proposed harvester as a function of the inner beam tip and external magnet displacements. The solid black line on the three-dimensional surface indicates the potential trajectory of the present system. **b** Projection of the potential trajectory on the $w_{t2} - U_t$ plane

first decreases to a local minimum, then increases again at larger displacements.

To better understand this behavior, Fig. 7b illustrates the projection of the potential trajectory onto the $w_{t2} - U_t$ plane for various spring stiffness values. For comparison, the potential curve of the cut-out harvester with a fixed external magnet is also depicted. It is evident that while the parameter K_3 influences the potential barrier height, it has no effect on the distance between the potential wells. As is seen, the potential energy of the proposed harvester with relatively high spring stiffness (e.g. $K_3 = 5000$ N/m) closely resembles that of the conventional cut-out BEH with a fixed magnet. Furthermore, a reduction in K_3 leads to a noticeable decrease in the potential energy barrier. When the spring stiffness is very low (e.g. $K_3 = 50$ N/m), the two wells tend to merge, potentially eliminating bistability. This underscores the importance of selecting an appropriate spring stiffness that sufficiently lowers the potential energy barrier while maintaining bistable behavior.

To clarify the role of the reduced potential barrier in enabling large inter-well oscillations, Fig. 8 presents time histories of the transverse displacement at the inner beam tip for both the conventional bistable cut-out PEH with a fixed magnet and the proposed MHEH, under identical excitation conditions (i.e., $f = 10$ Hz and $Z = 2.5\mathrm{m/s^2}$). As shown in Fig. 8a, the MHEH (i.e., the blue curve) exhibits large-amplitude oscillations, indicating inter-well motion. In contrast, the conventional harvester (i.e., the red curve) displays limited intra-well oscillations confined around a single equilibrium position. This contrast is further highlighted in the magnified view of the steady-state responses shown in Fig. 8b, where the wider oscillation range of the MHEH is evident.

To further explain this behavior, Fig. 8c and d present the potential energy corresponding to the above-mentioned configurations. The shaded regions in both figures represent the displacement ranges extracted from the time-domain responses in Fig. 8a and b. For the conventional harvester, the displacement range remains entirely within one potential well (see Fig. 8c), indicating that the system lacks sufficient energy to overcome the potential barrier. Conversely, the MHEH demonstrates a displacement range that extends across both wells (see Fig. 8d). This behavior is attributed to the adaptive reduction of the potential barrier caused by the oscillation of the external magnet. This inter-well motion significantly enhances the system's energy harvesting capability. Quantitatively, the conventional PEH generates an average power of 0.33 mW. In comparison, the MHEH achieves a significantly higher total output of 2.80 mW, which comprises 2.00 mW harvested via the piezoelectric component and an additional 0.80 mW from the electromagnetic mechanism.

Bifurcation of The Equilibrium Points

A critical factor influencing the bistable behavior of the proposed harvester is the distance between the two magnets [26]. Thus, the bifurcation of equilibrium points with the parameter d_0 is studied in this section. To do so, by setting all the time-dependent terms in Eq. (28) to zero, the equilibrium equations governing the fixed points of the system are obtained and then solved using MATLAB command fsolve.

Figure 9 depicts the variation of the inner beam equilibrium points with respect to the initial gap between the two magnets for different values of K_3. According to this figure, as the distance between the magnets decreases, the inner beam moves from a monostable state to a bistable one through a pitchfork bifurcation (PF). For instance, when $K_3 = 150$ N/m, the bifurcation point approximately occurs at $d_0 = 27.7$ mm. Thus, hiring initial gaps bigger than this value causes the harvester to operate as a monostable system. Also, it is evident that increasing the spring stiffness shifts the pitchfork point to the right.

To investigate this issue further, Fig. 10 illustrates the combination of K_3 and d_0 required for prompting high-energy inter-well oscillations, where the boundary between

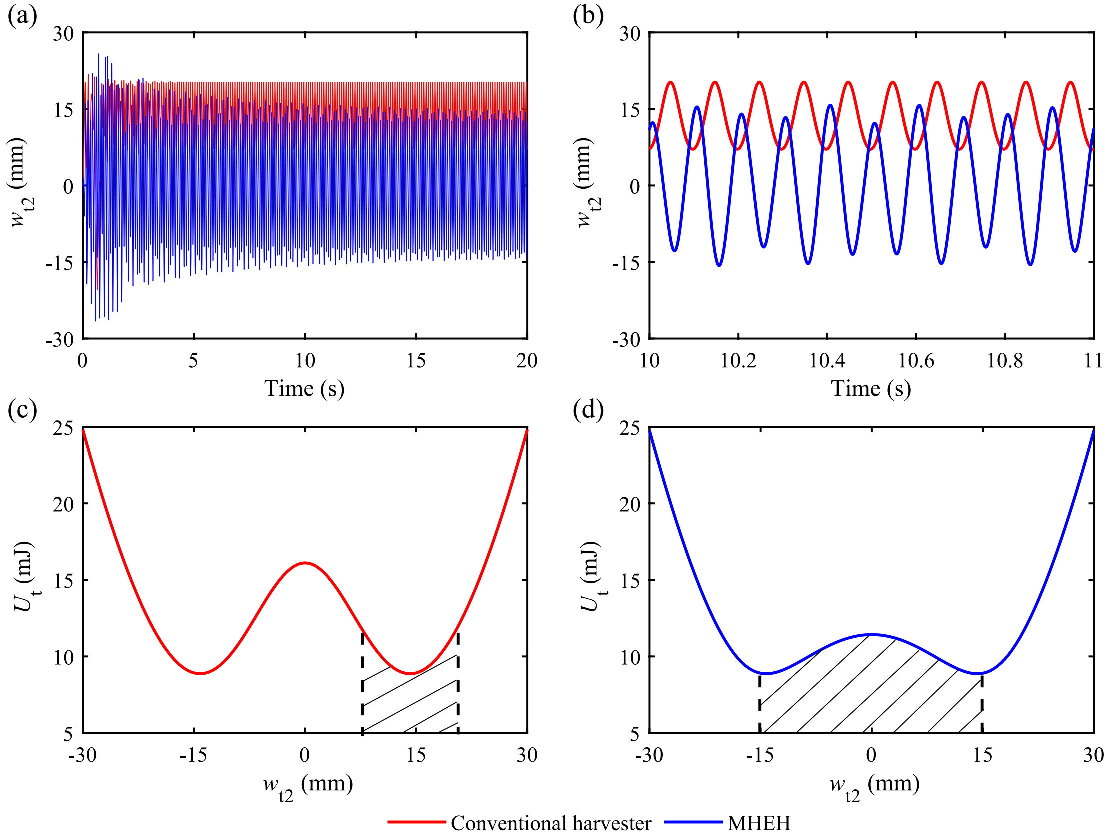

Fig. 8 **a** Time-domain displacement responses of the conventional bistable cut-out PEH and the proposed MHEH under the excitation frequency of 10 Hz and excitation intensity of 2.5 m/s^2; **b** magnified view of steady-state responses; (c-d) potential energy diagrams corresponding to each configuration, with shaded regions indicating displacement ranges

the monostable and bistable states is demonstrated by a blue line. For the points above this line (i.e., the yellow region), the harvester has two stable equilibria, while the system will lose its bistability when the values of K_3 and d_0 are selected from the region below the bistability blue line threshold (i.e., the light blue zone). As this figure demonstrates, the critical initial gap between the two magnets required for prompting bistability becomes smaller as the stiffness K_3 decreases. Given the fact that the lower the potential barrier, the easier the large amplitude vibrations occur, emphasizes that the stiffness of the magnetic oscillator along with the initial gaps between the two magnets should be selected very carefully to effectively lower the potential energy barrier while the bistability is kept.

Parametric Study

In designing the present hybrid harvester, obtaining the initial location of the induction coil relative to the magnetic oscillator is very important. Figure 11 depicts the variation of the electromagnetic coupling coefficient θ_{em} with respect to the external magnet location x_b. According to this figure, θ_{em} is a nonlinear function of x_b; because the magnetic field is variable. It is seen that the value of θ_{em} reaches the peak around $x_b = -1$ mm and $x_b = 18$ mm. According to Fig. 4 and the geometric properties of the coil presented in Table 1, these points correspond to the right and left edges of the coil, respectively. Furthermore, θ_{em} becomes zero at $x_b = 8.5$ mm, which corresponds to the center of the coil. On the other hand, from Eq. (17), the velocity of the magnetic oscillator is another factor that can affect the power scavenged from the electromagnetic converter. The velocity of the magnetic oscillator reaches the maximum value at its equilibrium position, under the harmonic oscillations. Thus, the equilibrium position of the external magnet is set to the right edge of the coil.

To evaluate the effectiveness of the MHEH, the output power and the operation bandwidth of the proposed harvester are compared with the conventional nonlinear cut-out energy harvester with a fixed external magnet. The initial gap between the magnets, d_0, is set to 23 mm. Also, the mechanical damping ratio of each oscillator is considered to be 0.8%. It is to be noted that the resistances of the piezoelectric and electromagnetic circuits are set to $R_1 = 800$ KΩ

Fig. 9 Bifurcation diagram of the inner beam tip

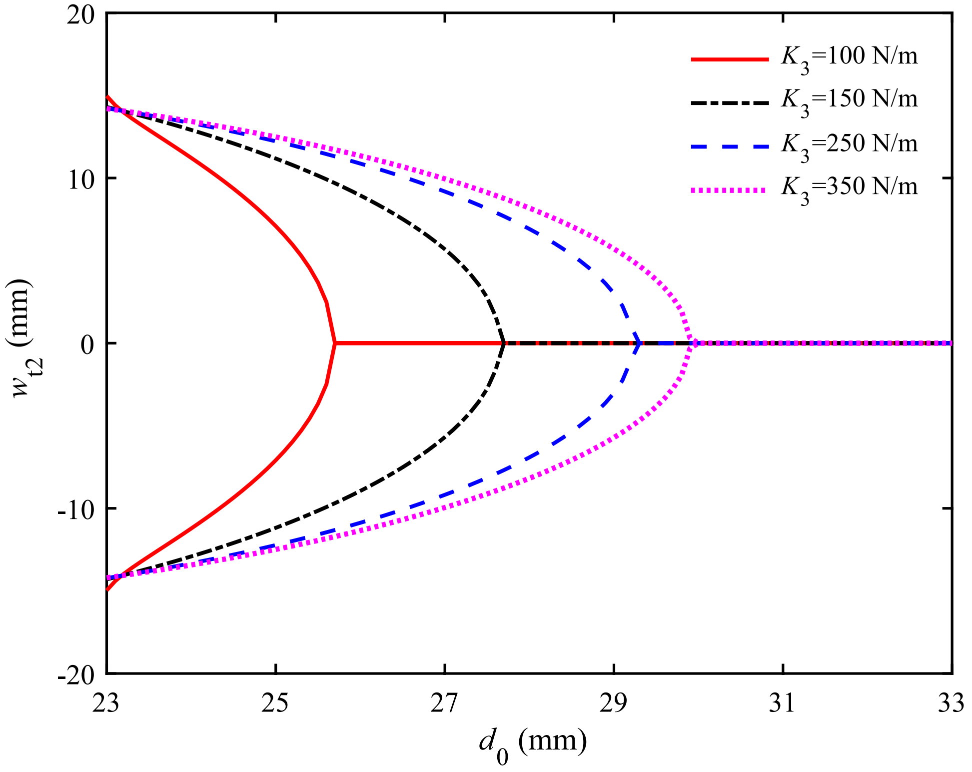

Fig. 10 Bistability criteria for the proposed harvester

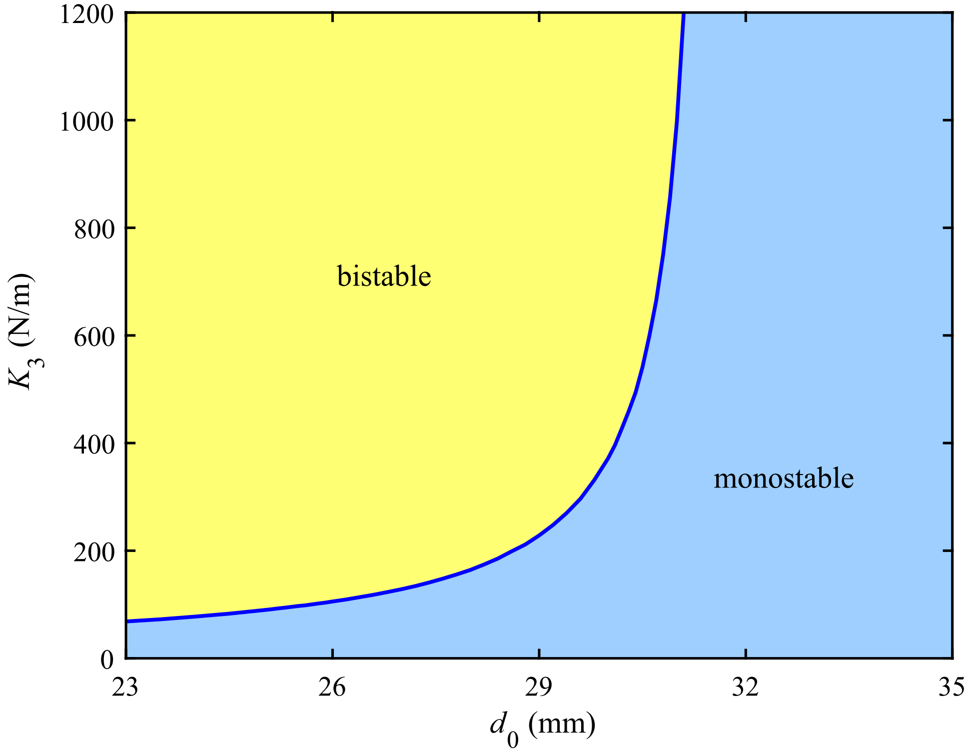

and $R_2 = 500\ \Omega$, respectively. As will be explained later in this study, these values are selected so that the harvester generates the maximum output power.

Figure 12 demonstrates the average power harvested by the two harvesters mentioned above as a function of the base excitation frequency and amplitude. The greater magnitude

Fig. 11 Electromagnetic coupling coefficient versus the position of the external magnet

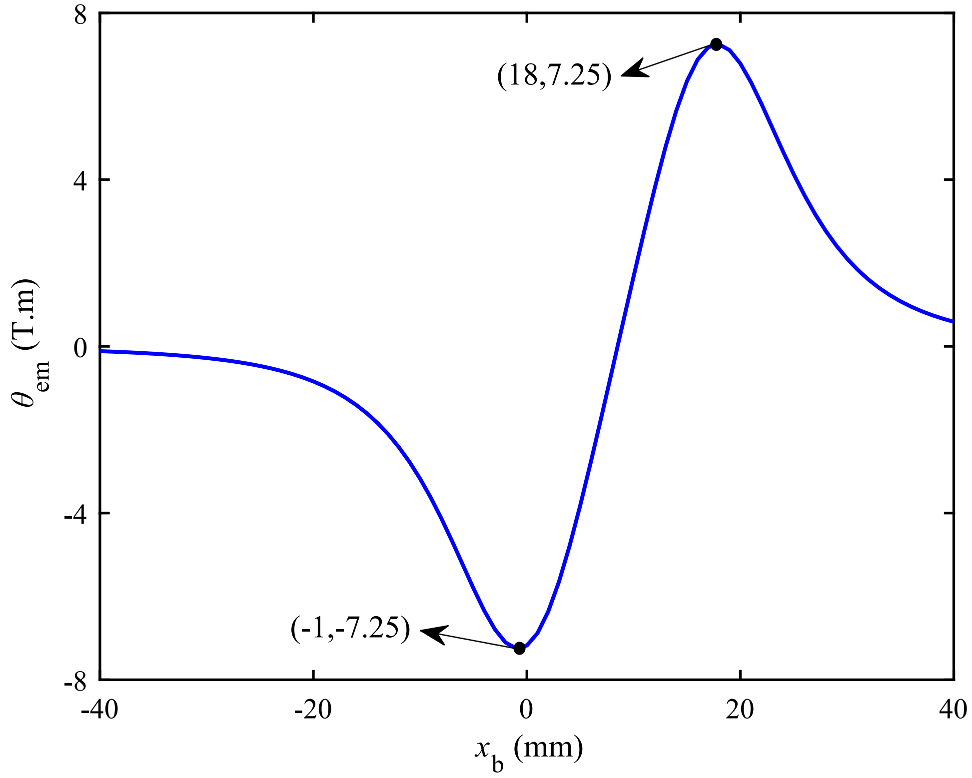

of the generated power is indicated by increasing the brightness of the contour. That is, the more the color varies from blue to yellow, the more power is scavenged. Therefore, as can be seen from this figure, the present MHEH exhibits remarkably greater performance over a much broader excitation range. For instance, under the acceleration amplitude of 5 m/s^2, the high-output region associated with the conventional harvester (i.e., the nonlinear cut-out harvester with a fixed external magnet), in which more than 4 mW electrical power is generated, covers the frequency range of 7—9.5 Hz. While the present MHEH under the same excitation level can harvest such a power, or even more, within the interval of 7–11.5 Hz. Moreover, it is notable that unlike the conventional system, the proposed harvester covers extremely low-amplitude excitations. That is, the high-output region associated with the present harvester starts from 1.5 m/s^2, while this range is limited to a zone starting from 3.5 m/s^2 for a system with the conventional design.

For a better comparison, the variation of the average output power versus the base acceleration is illustrated in Fig. 13 for two different values of the excitation frequency. Aside from the total power harvested by the conventional bistable cut-out beam and the proposed hybrid harvester, the power generated by the piezoelectric and electromagnetic transducers of the proposed platform is also separately presented in this figure. As is seen from Fig. 13a, when the excitation frequency is set to 8 Hz, which is lower than the frequencies corresponding to the linear

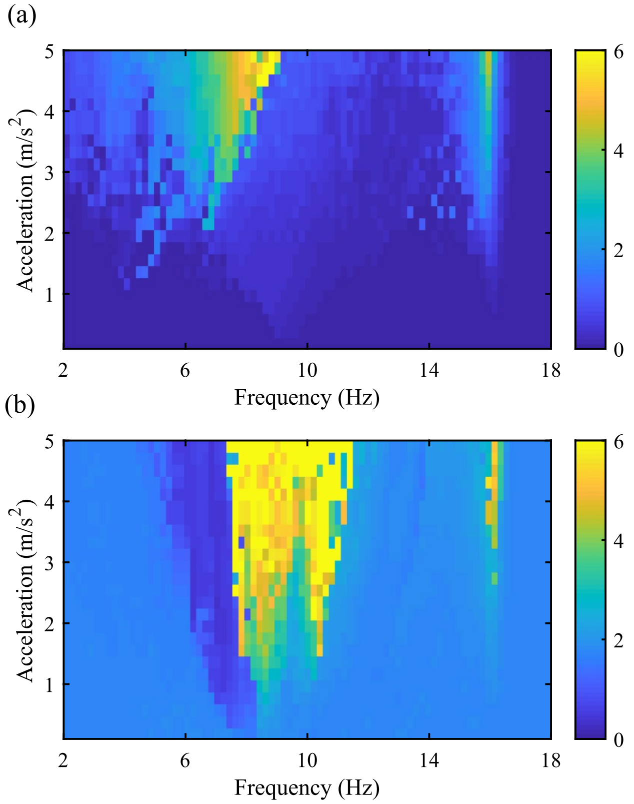

Fig. 12 Comparison of the average power harvested by **a** conventional bistable PEH with cut-out structure and **b** the proposed hybrid harvester

resonances of the cut-out beam, the electromagnetic transducer makes a major contribution to the total scavenged power compared to the piezoelectric converter. However, for an excitation frequency close to the natural frequencies of the cut-out structure (i.e., the case with $f = 11$ Hz), the role of the piezoelectric harvesting mechanism is more highlighted (see Fig. 13b). Even though when the acceleration intensity is very low, the electromagnetic converter can be more beneficial. In addition, Fig. 13 emphasizes that the proposed hybrid harvester can reach large-amplitude oscillations under extremely lower excitation accelerations at both excitation frequencies compared to the conventional cut-out PEH. This is supported by the sudden increase in the generated power, which indicates the onset of the inter-well oscillations. Also, it is evident that for both excitation frequencies, the proposed MHEH provides much greater power output, especially for lower base acceleration levels in comparison to the conventional harvester.

Figure 14 illustrates a comparison between the frequency response curves corresponding to the average output power associated with the conventional harvester and the present MHEH under two different acceleration intensities of 0.5 and 4.5 m/s^2. According to Fig. 14a, for a low-level excitation (i.e., $Z = 0.5\mathrm{m/s}^2$), where none of the conventional and present cases exhibit inter-well oscillations, the introduced MHEH generates significant amounts of power over a wider frequency range. As shown in this figure, the high performance of the proposed harvester under weak excitations is mainly due to the electrical power extracted from the induction coil. It is notable that the present system can generate the maximum power of 2.3 mW, which is about 9

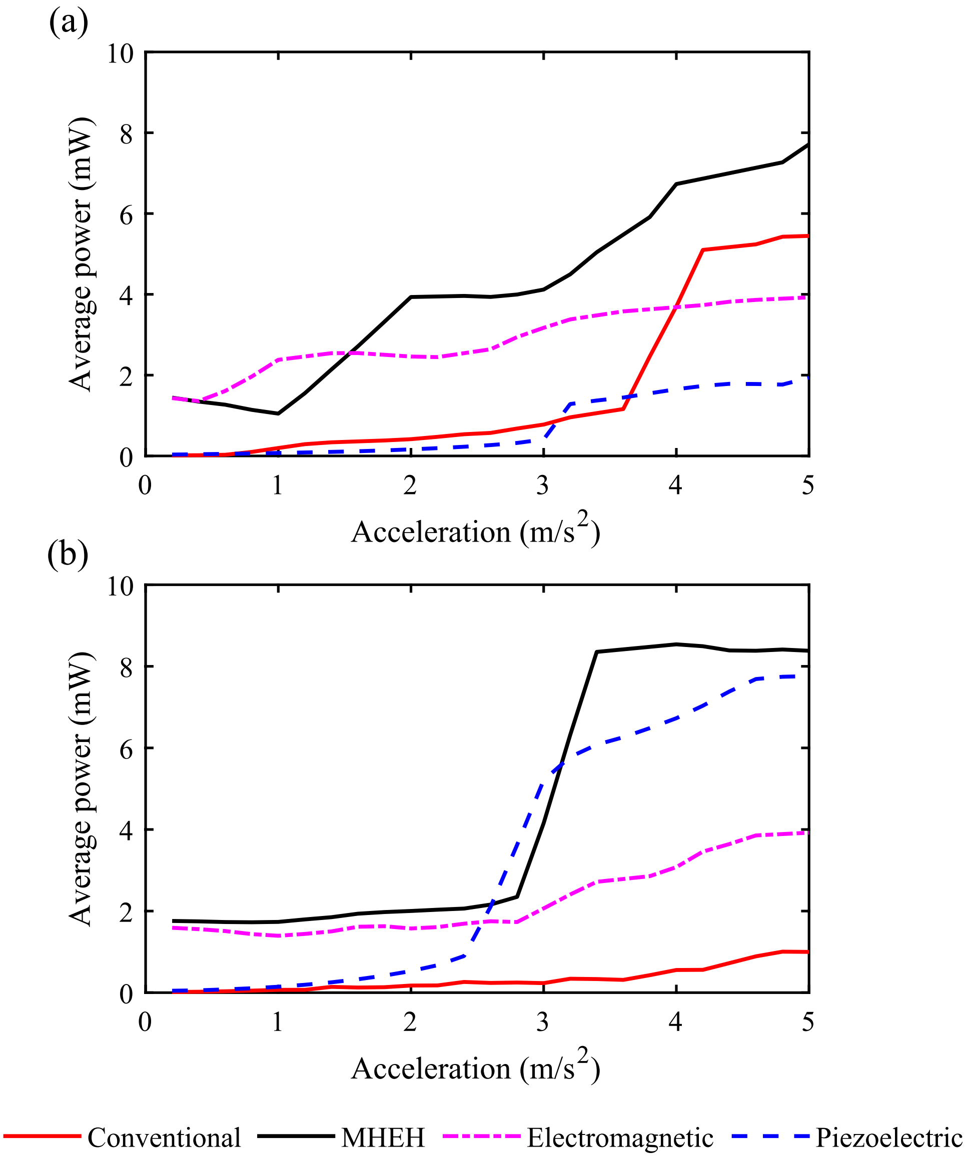

Fig. 13 The average power harvested by the conventional bistable cut-out PEH, electromagnetic and piezoelectric parts of the proposed harvester separately and their combination as an MHEH under the excitation frequency of **a** 8 Hz and **b** 11 Hz

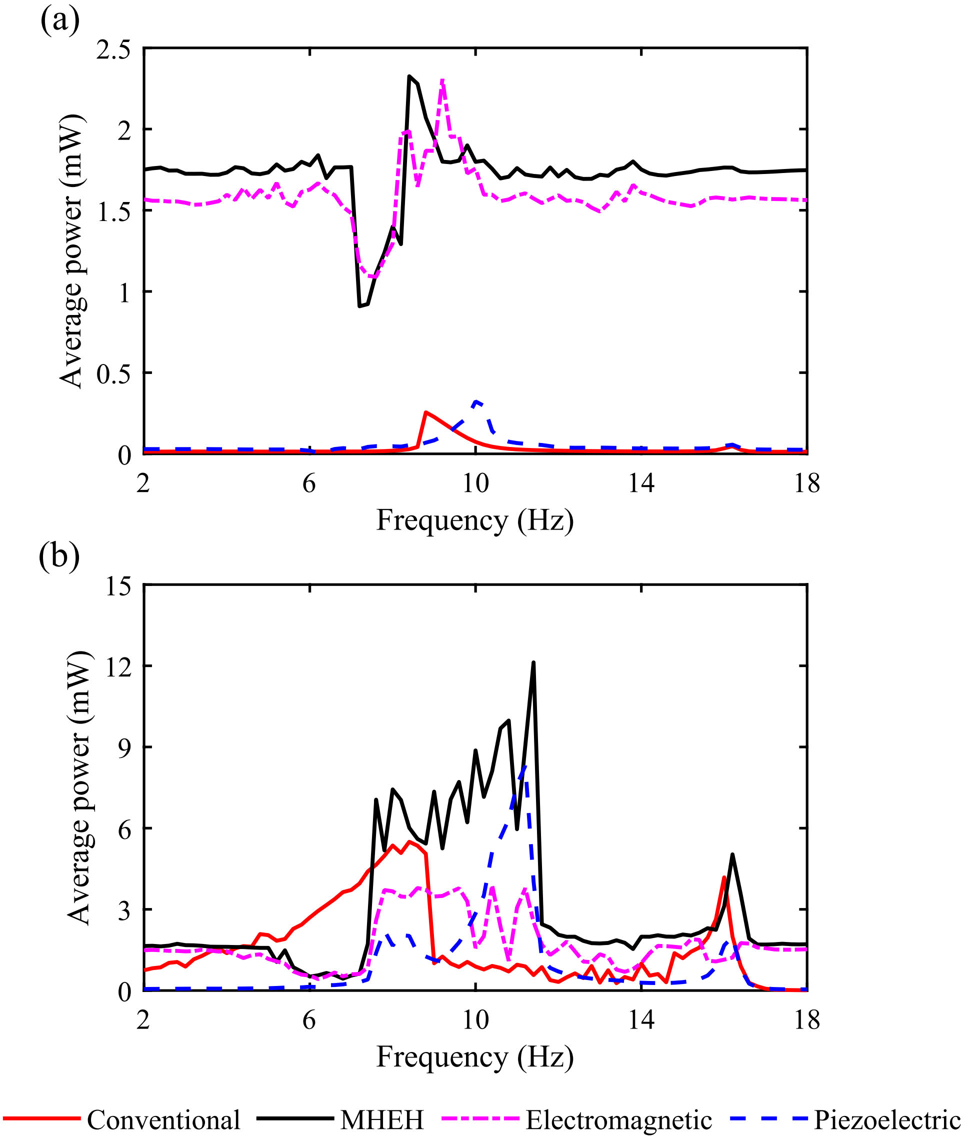

Fig. 14 The average power harvested by the conventional bistable cut-out PEH, electromagnetic and piezoelectric parts of the proposed harvester separately and their combination as an MHEH under the excitation intensity of **a** 0.5 m/s^2 and **b** 4.5 m/s^2

times greater than that of the conventional harvester with a fixed magnet.

For the high-level excitation case (i.e., $Z = 4.5\mathrm{m/s^2}$), in which the inter-well oscillations are activated in both the present and conventional systems, the high-output region associated with the proposed platform is broadened over a frequency range of 7.5–11.5 Hz, which is about 90% wider than that of the conventional cut-out PEH. Furthermore, the present design is capable of generating a maximum power of 12.13 mW, which is 118% higher than that of the conventional harvester. According to Fig. 14b, while the conventional PEH performs better within the 4.5–7.5 Hz frequency range, the results highlight the superiority of the MHEH in terms of offering higher output power over a broader frequency range.

As demonstrated in Sect."Potential Energy Surface", the potential energy analysis revealed that variations in the magnetic oscillator stiffness can significantly influence the bistability condition of the proposed harvester. Therefore, it is essential to investigate the effect of spring stiffness on the average power generated by the MHEH. Figure 15 depicts the average output power of the present design for different spring stiffness values under a base acceleration of Z=4.5 m/s^2. Based on the earlier potential energy analysis, three representative stiffness values, 50, 200, and 5000 N/m, are selected to represent low, moderate, and high stiffness cases, respectively. Given the results provided in Fig. 7, the black dash-dotted line in Fig. 15, which corresponds to the soft spring case, represents a monostable motion. Therefore, as observed, the total harvested power in this case is reduced. As the stiffness K_3 increases to 200 N/m, both the output power and the working frequency range of the harvester significantly improve. This observation is attributed to the combined effects of a lowered potential barrier and the

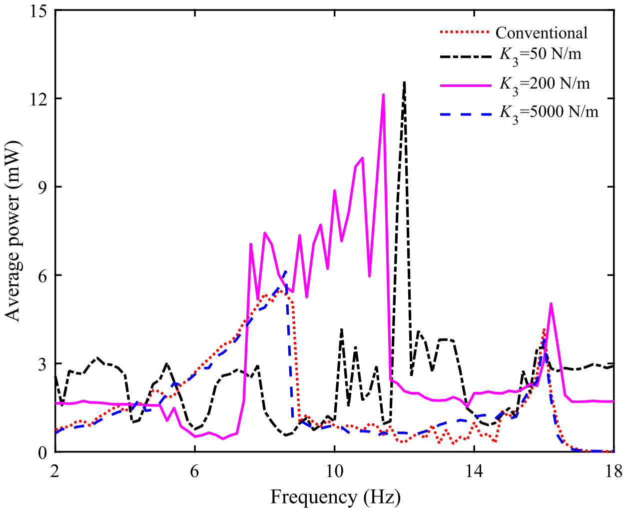

Fig. 15 The influence of the magnetic oscillator stiffness on the output power generated by the hybrid harvester

multi-frequency configuration in the current design. Finally, for the high stiffness case (i.e., the case with $K_3 = 5000$ N/m), the system's behavior closely resembles that of a conventional harvester with a fixed magnet, as indicated by the red dotted line in Fig. 15.

Figure 16 illustrates the influence of the mass of the magnetic oscillator on the average power frequency response curve. As can be seen from this figure, increasing M_3 shifts the high-output region toward lower frequencies, with minimal impact on the operational bandwidth. Moreover, the value of M_3 influences the maximum harvested power. Hence, precise adjustment of the magnetic mass allows for fine-tuning of the operational frequency range, thereby maximizing the harvested power. As illustrated in the figure, setting the mass of the external magnet to 30 gr enables the system to harvest a substantial amount of power at lower frequencies.

To harvest the maximum possible power, the resistances of the piezoelectric and magnetic circuits should be optimized. To this end, Table 2 represents the maximum average powers corresponding to different combinations of these resistances.

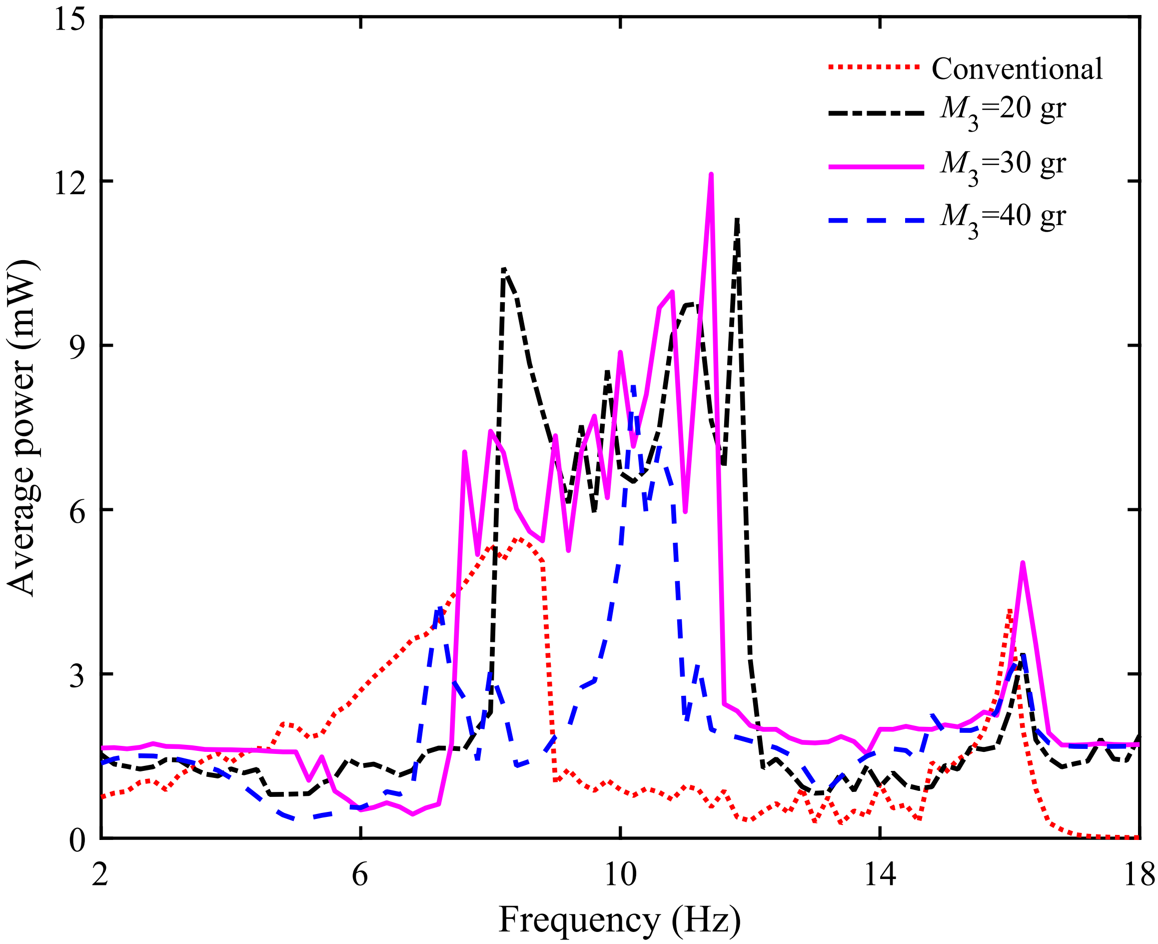

Fig. 16 The influence of the magnetic oscillator mass on the output power generated by the hybrid harvester

As this table demonstrates, the maximum harvested power initially increases with rising R_1, reaches a peak, and subsequently decreases. The findings suggest that variations in coil resistance do not influence this overall trend and can not drastically affect the maximum power. It is to be noted that these results are consistent with the findings reported by Khaghanifard et al. [45], thereby confirming the accuracy of the current study. It is worth mentioning that the maximum harvested power of 12.13 mW was recorded at $R_1 = 800$ KΩ and $R_2 = 500$ Ω. According to Fig. 14, this is 118% higher than that of the conventional harvester with the same properties.

In order to better compare the performance of the proposed energy harvester with other designs reported in the previous studies, it is necessary to define a figure of merit (FOM). This FOM should incorporate key parameters such as the harvester's dimensions, excitation level, effective bandwidth, and generated power. A FOM was previously introduced in [41], which is expressed as

$$FOM = \frac{BW \times P_{avg}}{U^2 \times V_{tot}}, \tag{33}$$

where U and V_{tot} are the amplitude of the applied excitation and the total volume of the harvester, respectively. BW represents the normalized bandwidth and is defined as $BW = \left(f_R - f_L\right)/f_C$, where f_R and f_L denote the frequencies at which the harvester's power reaches half of its maximum value, and f_C refers to the central frequency of this bandwidth. Also, P_{avg} denotes the average output power over the effective bandwidth.

Table 2 The maximum output power versus the piezoelectric (R_1) and magnetic (R_2) resistances

R_{1}(**kΩ**)	$P_{\max}$ (mW)			
	$R_2 = 400\Omega$	$R_2 = 500\Omega$	$R_2 = 600\Omega$	$R_2 = 700\Omega$
200	9.543	7.132	7.419	6.489
400	9.664	9.036	8.666	11.020
600	11.760	9.252	11.985	12.010
800	10.370	12.130	11.960	11.780
1000	10.140	11.420	11.260	9.503
1200	10.780	10.600	10.400	8.617
1400	9.976	9.825	9.208	8.956

Table 3 provides the FOM values for the proposed hybrid harvester as well as other previously reported harvesters with cut-out configurations. According to this table, the present system outperforms all other designs in terms of FOM, indicating a superior energy harvesting capability. The proposed MHEH achieves a FOM of 2.779 W.s^2/m^4, representing a 169% increase over the conventional bistable PEH, a 2953.8% increase relative to the monostable configuration [40], a 1574.1% increase compared with the quad-stable system [41], and a 1296.5% increase versus the nonlinear harvester presented in [42]. These substantial enhancements arise from the superior average power output and wider operational bandwidth of the MHEH. This analysis highlights that employing bistability along with the variable potential barrier concept can significantly enhance the performance of energy harvesters compared to traditional methods.

Conclusions

The present paper developed a novel bistable multi-frequency hybrid energy harvester by combining piezoelectric and electromagnetic transduction mechanisms. The nonlinear coupled equations of motion were obtained employing a hybrid procedure including the Ritz method, and solved numerically. Potential and bifurcation analyses revealed that key parameters, such as the spring stiffness and the initial gap between the magnets, can affect the shape of the equilibrium path. Most importantly, a bistability criterion was established, outlining the required combination of the system parameters to induce inter-well oscillations.

A comparative study showed the supremacy of the introduced harvester over the conventional magnetically bistable PEH in terms of the higher generated power over a broader range of excitations. The proposed hybrid harvester can offer an operational bandwidth of 4 Hz (i.e., 7.5–11.5 Hz) under 4.5 m/s^2 excitation, which is increased by 90% compared

Table 3 Performance comparison of this work with several previously reported harvesters from the literature

Reference	Main feature	Excitation (m/s^2)	$f_R - f_L$(Hz)	FOM (W.s^2/m^4)	MHEH improvement relative to reference (%)
Wu et al. [40]	Cut-out, monostable	2	5	0.091	2953.8
Zayed et al. [41]	Cut-out, Quad-stable	3	7.3	0.166	1574.1
Tian et al. [42]	Cut-out, Nonlinear	3	12.8	0.199	1296.5
This work	Cut-out, bistable	4.5	1.7	1.033	169
This work	Cut-out, variable barrier bistable	4.5	4	2.779	_

to the conventional system. Also, the present platform can generate a maximum power of almost 12 mW, representing an approximate 118% increase over the conventional system. In addition, introducing a self-decreasing potential barrier enables the system to initiate inter-well oscillations at substantially lower excitation intensities than those required by the conventional harvester.

Moreover, a FOM was introduced to evaluate the performance of the present hybrid harvester compared to other cut-out-based harvesters reported in the literature. According to this analysis, the proposed MHEH exhibits a 169% improvement in energy harvesting efficiency compared to the conventional bistable PEH.

Appendix A

This section provides the mode-shapes of the cut-out structure which appeared in Eq. (26). It is notable that since the admissible basis function in the Ritz method should be selected so that all the essential boundary conditions are satisfied, only the cut-out structure without the piezoelectric layers is considered. In addition, bearing in mind that the ambient excitation typically involves low frequencies, the first mode-shape of each beam is considered. Thus, in accordance with the previously given mathematical model, the transverse equation governing each beam is simplified to [54]

$$E_sI_i\frac{\partial^4\hat{w}_i\left(\hat{x}_i,\hat{t}\right)}{\partial\hat{x}_i^4}+m_i\frac{\partial^2\hat{w}_i\left(\hat{x}_i,\hat{t}\right)}{\partial\hat{t}^2}=0, \tag{A.1}$$

where the stiffness and mass per unit length of each beam are given by

$$\begin{gathered}m_1=2\rho_sb_{s1}h_{s1},\\ E_sI_1=2\left(\tfrac{1}{12}\right)E_sb_{s1}h_{s1}^3\ \text{for } 0\le\hat{x}_1\le L_1,\\ m_2=\rho_sb_{s2}h_{s2},\\ E_sI_2=\tfrac{1}{12}E_sb_{s2}h_{s2}^3\ \text{for } 0\le\hat{x}_2\le L_2.\end{gathered} \tag{A.2}$$

Assuming simple harmonic motion for the system, the transverse deflection of the structure is taken as $\hat{w}\left(\hat{x}_i,t\right)=\varphi(\hat{x})e^{j\omega t}$ where $\varphi(\hat{x})$ is the system mode-shape and ω is its corresponding natural frequency. The mode-shape of the whole system can be divided into two parts corresponding to the outer and inner beams. So, the resulting eigenvalue problem for each part is

$$\begin{aligned}&\varphi(\hat{x})=\varphi_1\left(\hat{x}_1\right), && EI_1\varphi_1^{iv}-m_1\omega^2\varphi_1=0 && \text{for } 0\le\hat{x}_1\le L_1,\\ &\varphi(\hat{x})=\varphi_2\left(\hat{x}_2\right), && EI_2\varphi_2^{iv}-m_2\omega^2\varphi_2=0 && \text{for } 0\le\hat{x}_2\le L_2.\end{aligned} \tag{A.3}$$

The fixed boundary conditions at the beginning of the outer beam (i.e., at $\hat{x}_1=0$) are expressed as

$$\varphi_1(0)=0,\ \ \varphi_1'(0)=0. \tag{A.4}$$

The boundary conditions at the end of the outer beam, which coincides the beginning of the inner beam (i.e., at $\hat{x}_1=L_1$ and $\hat{x}_2=0$), are as below

$$\begin{gathered}\varphi_1\left(L_1\right)=-\varphi_2(0),\ \ \varphi_1'\left(L_1\right)=\varphi_2'(0),\\ EI_1\varphi_1''\left(L_1\right)=EI_2\varphi_2''(0),\quad EI_1\varphi_1'''\left(L_1\right)+\omega^2M_{t1}\varphi_1\left(L_1\right)=-EI_2\varphi_2''(0).\end{gathered} \tag{A.5}$$

The boundary conditions at the end of the inner beam (i.e., at $\hat{x}_2=L_2$) are given by

$$EI_2\varphi_2''\left(L_2\right)=0,\ \ EI_2\varphi_2'''\left(L_2\right)+\omega^2M_{t2}\varphi_2\left(L_2\right)=0. \tag{A.6}$$

The solution of Eq. (A.3) is [43]

$$\varphi_{ir}=A_{ir}\sin\left(\frac{\beta_{ir}\hat{x}_i}{L_i}\right)+B_{ir}\cos\left(\frac{\beta_{ir}\hat{x}_i}{L_i}\right)+C_{ir}\sinh\left(\frac{\beta_{ir}\hat{x}_i}{L_i}\right)+D_{ir}\cosh\left(\frac{\beta_{ir}\hat{x}_i}{L_i}\right), \tag{A.7}$$

where A_{ir}, B_{ir}, C_{ir}, and D_{ir} are some unknowns which can be found through satisfying the boundary conditions given in Eqs. (A.4) to (A.6). Also, the coefficients β_{1r} and β_{2r} are related to each other by $\beta_{2r}=\sqrt[4]{\frac{EI_1m_2}{EI_2m_1}}\beta_{1r}$.

Appendix B

The non-dimensional coefficients appearing in Eqs. (28) are defined as

$$\begin{gathered}f_1=\tfrac{2E_{s1}A_{s1}T^2}{M_{t1}L_1},\\ g_1=\frac{\left(E_{s2}A_{s2}+E_pA_p\frac{L_p}{L_2}\right)T^2}{M_{t2}L_2},\quad g_2=-\tfrac{B_{s2}L_1T^2}{M_{t2}L_2^3}\int_0^1\varphi_{21}''dx_2-\tfrac{B_pL_1T^2}{M_{t2}L_2^3}\int_0^{\frac{L_p}{L_2}}\varphi_{21}''dx_2,\\ g_3=-\tfrac{B_{s2}L_1T^2}{M_{t2}L_2^3}\int_0^1\varphi_{22}''dx_2-\tfrac{B_pL_1T^2}{M_{t2}L_2^3}\int_0^{\frac{L_p}{L_2}}\varphi_{22}''dx_2,\quad g_4=\tfrac{A_eL_pV^*T^2}{M_{t2}L_2^2h_p},\\ g_5=\tfrac{T^2}{M_{t2}L_2},\end{gathered} \tag{B.1}$$

$$h_1=\frac{c_3T}{M_3},\quad h_2=\frac{K_3T^2}{M_3},\quad h_3=-\frac{T^2}{M_3L_1},\quad h_4=\frac{\theta_{em}I^*T^2}{M_3L_1},$$

$$p_1 = \frac{d_3}{d_1}, \quad p_2 = \frac{1}{d_1}\left(\frac{2c_1L_1^2}{T^2}\int_0^1 \varphi_{11}^2 dx_1 + \frac{c_1L_1L_2}{T^2}\int_0^1 \varphi_{21}^2 dx_2\right),$$

$$p_3 = \frac{1}{d_1}\left(\frac{2c_1L_1^2}{T^2}\int_0^1 \varphi_{11}\varphi_{12} dx_1 + \frac{c_1L_1L_2}{T^2}\int_0^1 \varphi_{21}\varphi_{22} dx_2\right),$$

$$p_4 = \frac{1}{d_1}\left[2\frac{C_{s1}}{L_1^2}\int_0^1 {\varphi_{11}''}^2 dx_1 + \frac{C_{s2}L_1}{L_2^3}\int_0^1 {\varphi_{21}''}^2 dx_2 + \frac{C_{p2}L_1}{L_2^3}\int_0^{\frac{L_p}{L_2}} {\varphi_{21}''}^2 dx_2\right.$$

$$+\frac{B_{s2}L_1}{L_2^3\left(E_{s2}A_{s2} + E_pA_p\right)}\int_0^{\frac{L_p}{L_2}} \varphi_{21}'' dx_2\left(B_{s2}\int_0^1 \varphi_{21}'' dx_2 + B_p\int_0^{\frac{L_p}{L_2}} \varphi_{21}'' dx_2\right)$$

$$+\frac{B_pL_1}{L_2^3\left(E_{s2}A_{s2} + E_pA_p\right)}\int_0^{\frac{L_p}{L_2}} \varphi_{21}'' dx_2\left(B_{s2}\int_0^1 \varphi_{21}'' dx_2 + B_p\int_0^{\frac{L_p}{L_2}} \varphi_{21}'' dx_2\right)$$

$$-\frac{B_{s2}L_1}{L_2^3\left(E_{s2}A_{s2} + E_pA_p\right)}\left(B_{s2}\int_0^{\frac{L_p}{L_2}} {\varphi_{21}''}^2 dx_2 + B_p\int_0^{\frac{L_p}{L_2}} {\varphi_{21}''}^2 dx_2\right)$$

$$\left.-\frac{B_pL_1}{L_2^3\left(E_{s2}A_{s2} + E_pA_p\right)}\left(B_{s2}\int_0^{\frac{L_p}{L_2}} {\varphi_{21}''}^2 dx_2 + B_p\int_0^{\frac{L_p}{L_2}} {\varphi_{21}''}^2 dx_2\right)\right],$$

$$p_5 = \frac{1}{d_1}\left[2\frac{C_{s1}}{L_1^2}\int_0^1 \varphi_{11}''\varphi_{12}'' dx_1 + \frac{C_{s2}L_1}{L_2^3}\int_0^1 \varphi_{21}''\varphi_{22}'' dx_2 + \frac{C_{p2}L_1}{L_2^3}\int_0^{\frac{L_p}{L_2}} \varphi_{21}''\varphi_{22}'' dx_2\right.$$

$$+\frac{B_{s2}L_1}{L_2^3\left(E_{s2}A_{s2} + E_pA_p\right)}\int_0^{\frac{L_p}{L_2}} \varphi_{21}'' dx_2\left(B_{s2}\int_0^1 \varphi_{22}'' dx_2 + B_p\int_0^{\frac{L_p}{L_2}} \varphi_{22}'' dx_2\right)$$

$$+\frac{B_pL_1}{L_2^3\left(E_{s2}A_{s2} + E_pA_p\right)}\int_0^{\frac{L_p}{L_2}} \varphi_{21}'' dx_2\left(B_{s2}\int_0^1 \varphi_{22}'' dx_2 + B_p\int_0^{\frac{L_p}{L_2}} \varphi_{22}'' dx_2\right)$$

$$-\frac{B_{s2}L_1}{L_2^3\left(E_{s2}A_{s2} + E_pA_p\right)}\left(B_{s2}\int_0^{\frac{L_p}{L_2}} \varphi_{21}''\varphi_{22}'' dx_2 + B_p\int_0^{\frac{L_p}{L_2}} \varphi_{21}''\varphi_{22}'' dx_2\right)$$

$$\left.-\frac{B_pL_1}{L_2^3\left(E_{s2}A_{s2} + E_pA_p\right)}\left(B_{s2}\int_0^{\frac{L_p}{L_2}} \varphi_{21}''\varphi_{22}'' dx_2 + B_p\int_0^{\frac{L_p}{L_2}} \varphi_{21}''\varphi_{22}'' dx_2\right)\right],$$

$$p_6 = \frac{1}{d_1}\left[-\frac{\left(B_{s2} + B_p\right)\left(E_{s2}A_{s2} + E_pA_p\frac{L_p}{L_2}\right)}{L_2\left(E_{s2}A_{s2} + E_pA_p\right)}\int_0^{\frac{L_p}{L_2}} \varphi_{21}'' dx_2\right],$$

$$p_7 = \frac{1}{d_1}\left[\frac{B_eV^*}{h_p}\int_0^{\frac{L_p}{L_2}} \varphi_{21}'' dx_2 - \frac{B_{s2}\left(\frac{L_p}{L_2} - 1\right)}{L_2\left(E_{s2}A_{s2} + E_pA_p\right)}\frac{A_eV^*}{h_p}\int_0^{\frac{L_p}{L_2}} \varphi_{21}'' dx_2\right.$$

$$\left.-\frac{B_p\left(\frac{L_p}{L_2} - 1\right)}{L_2\left(E_{s2}A_{s2} + E_pA_p\right)}\frac{A_eV^*}{h_p}\int_0^{\frac{L_p}{L_2}} \varphi_{21}'' dx_2\right], \quad p_8 = -\frac{\varphi_{21}}{d_1},$$

$$p_9 = \frac{1}{d_1}\left[\frac{2\rho_{s1}A_{s1}L_1^2}{T^2}\int_0^1 \varphi_{11} dx_1 - \frac{\rho_{s2}A_{s2}L_1L_2}{T^2}\int_0^1 \varphi_{21} dx_2\right.$$

$$\left.-\frac{\rho_pA_pL_1L_2}{T^2}\int_0^{\frac{L_p}{L_2}} \varphi_{21}^2 dx_2 + \frac{M_{t1}L_1}{T^2}\varphi_{11}(1) - \frac{M_{t2}L_1}{T^2}\varphi_{21}(1)\right],$$

$$q_1 = \frac{d_3}{d_2}, \quad q_2 = \frac{1}{d_2}\left(\frac{2c_1L_1^2}{T^2}\int_0^1 \varphi_{11}\varphi_{12} dx_1 + \frac{c_1L_1L_2}{T^2}\int_0^1 \varphi_{21}\varphi_{22} dx_2\right),$$

$$q_3 = \frac{1}{d_2}\left(\frac{2c_1L_1^2}{T^2}\int_0^1 {\varphi_{12}}^2 dx_1 + \frac{c_1L_1L_2}{T^2}\int_0^1 {\varphi_{22}}^2 dx_2\right),$$

$$q_4 = \frac{1}{d_2}\left[2\frac{C_{s1}}{L_1^2}\int_0^1 \varphi_{11}''\varphi_{12}'' dx_1 + \frac{C_{s2}L_1}{L_2^3}\int_0^1 \varphi_{21}''\varphi_{22}'' dx_2 + \frac{C_pL_1}{L_2^3}\int_0^{\frac{L_p}{L_2}} \varphi_{21}''\varphi_{22}'' dx_2\right.$$

$$+\frac{B_{s2}L_1}{L_2^3\left(E_{s2}A_{s2} + E_pA_p\right)}\int_0^{\frac{L_p}{L_2}} \varphi_{22}'' dx_2\left(B_{s2}\int_0^1 \varphi_{21}'' dx_2 + B_p\int_0^{\frac{L_p}{L_2}} \varphi_{21}'' dx_2\right)$$

$$+\frac{B_pL_1}{L_2^3\left(E_{s2}A_{s2} + E_pA_p\right)}\int_0^{\frac{L_p}{L_2}} \varphi_{22}'' dx_2\left(B_{s2}\int_0^1 \varphi_{21}'' dx_2 + B_p\int_0^{\frac{L_p}{L_2}} \varphi_{21}'' dx_2\right)$$

$$-\frac{B_{s2}L_1}{L_2^3\left(E_{s2}A_{s2} + E_pA_p\right)}\left(B_{s2}\int_0^{\frac{L_p}{L_2}} \varphi_{21}''\varphi_{22}'' dx_2 + B_p\int_0^{\frac{L_p}{L_2}} \varphi_{21}''\varphi_{22}'' dx_2\right)$$

$$\left.-\frac{B_pL_1}{L_2^3\left(E_{s2}A_{s2} + E_pA_p\right)}\left(B_{s2}\int_0^{\frac{L_p}{L_2}} \varphi_{21}''\varphi_{22}'' dx_2 + B_p\int_0^{\frac{L_p}{L_2}} \varphi_{21}''\varphi_{22}'' dx_2\right)\right],$$

$$q_5 = \frac{1}{d_2}\left[2\frac{C_{s1}}{L_1^2}\int_0^1 {\varphi_{12}''}^2 dx_1 + \frac{C_{s2}L_1}{L_2^3}\int_0^1 {\varphi_{22}''}^2 dx_2 + \frac{C_pL_1}{L_2^3}\int_0^{\frac{L_p}{L_2}} {\varphi_{22}''}^2 dx_2\right.$$

$$+\frac{B_{s2}L_1}{L_2^3\left(E_{s2}A_{s2}+E_pA_p\right)}\int_0^{\frac{L_p}{L_2}}\varphi''_{22}dx_2\left(B_{s2}\int_0^1\varphi''_{22}dx_2+B_p\int_0^{\frac{L_p}{L_2}}\varphi''_{22}dx_2\right)$$

$$+\frac{B_pL_1}{L_2^3\left(E_{s2}A_{s2}+E_pA_p\right)}\int_0^{\frac{L_p}{L_2}}\varphi''_{22}dx_2\left(B_{s2}\int_0^1\varphi''_{22}dx_2+B_p\int_0^{\frac{L_p}{L_2}}\varphi''_{22}dx_2\right)$$

$$-\frac{B_{s2}L_1}{L_2^3\left(E_{s2}A_{s2}+E_pA_p\right)}\left(B_{s2}\int_0^{\frac{L_p}{L_2}}{\varphi''_{22}}^2dx_2+B_p\int_0^{\frac{L_p}{L_2}}{\varphi''_{22}}^2dx_2\right)$$

$$-\frac{B_pL_1}{L_2^3\left(E_{s2}A_{s2}+E_pA_p\right)}\left(B_{s2}\int_0^{\frac{L_p}{L_2}}{\varphi''_{22}}^2dx_2+B_p\int_0^{\frac{L_p}{L_2}}{\varphi''_{22}}^2dx_2\right)\Bigg],$$

$$q_6=\frac{1}{d_2}\left[-\frac{\left(B_{s2}+B_p\right)\left(E_{s2}A_{s2}+E_pA_p\frac{L_p}{L_2}\right)}{L_2\left(E_{s2}A_{s2}+E_pA_p\right)}\int_0^{\frac{L_p}{L_2}}\varphi''_{22}dx_2\right],$$

$$q_7=\frac{1}{d_2}\left[\frac{B_eV^*}{h_p}\int_0^{\frac{L_p}{L_2}}\varphi''_{22}dx_2-\frac{B_{s2}\left(\frac{L_p}{L_2}-1\right)}{L_2\left(E_{s2}A_{s2}+E_pA_p\right)}\frac{A_eV^*}{h_p}\int_0^{\frac{L_p}{L_2}}\varphi''_{22}dx_2\right.$$

$$\left.-\frac{B_p\left(\frac{L_p}{L_2}-1\right)}{L_2\left(E_{s2}A_{s2}+E_pA_p\right)}\frac{A_eV^*}{h_p}\int_0^{\frac{L_p}{L_2}}\varphi''_{22}dx_2\right],\quad q_8=-\frac{\varphi_{22}}{d_2},$$

$$q_9=\frac{1}{d_2}\left[\frac{2\rho_{s1}A_{s1}L_1^2}{T^2}\int_0^1\varphi_{12}dx_1-\frac{\rho_{s2}A_{s2}L_1L_2}{T^2}\int_0^1\varphi_{22}dx_2\right.$$

$$\left.-\frac{\rho_pA_pL_1L_2}{T^2}\int_0^{\frac{L_p}{L_2}}\varphi_{22}^2dx_2+\frac{M_{t1}L_1}{T^2}\varphi_{12}(1)-\frac{M_{t2}L_1}{T^2}\varphi_{22}(1)\right],$$

$$r_1=\frac{A_eh_p}{\varepsilon_{33}A_pV^*},\quad r_2=\frac{B_eh_pL_1}{\varepsilon_{33}A_pL_pL_2V^*}\int_0^{\frac{L_p}{L_2}}\varphi''_{21}dx_2,$$

$$r_3=\frac{B_eh_pL_1}{\varepsilon_{33}A_pL_pL_2V^*}\int_0^{\frac{L_p}{L_2}}\varphi''_{22}dx_2,\quad r_4=\frac{h_p^2T}{\varepsilon_{33}A_pL_pR_1},$$

$$s_1=\frac{\left(R_c+R_2\right)T}{L_c},\quad s_2=-\theta_{em},$$

in which

$$\begin{aligned}d_1={}&\tfrac{2\rho_{s1}A_{s1}L_1^2}{T^2}\int_0^1\varphi_{11}^2dx_1+\tfrac{\rho_{s2}A_{s2}L_1L_2}{T^2}\int_0^1\varphi_{21}^2dx_2+\tfrac{\rho_pA_pL_1L_2}{T^2}\int_0^{\frac{L_p}{L_2}}\varphi_{21}^2dx_2\\&+\tfrac{M_{t1}L_1}{T^2}\varphi_{11}^2(1)+\tfrac{I_{t1}}{L_1T^2}{\varphi'_{11}}^2(1)+\tfrac{M_{t2}L_1}{T^2}\varphi_{21}^2(1)+\tfrac{I_{t2}L_1}{L_2^2T^2}{\varphi'_{21}}^2(1),\\d_2={}&\tfrac{2\rho_{s1}A_{s1}L_1^2}{T^2}\int_0^1\varphi_{12}^2dx_1+\tfrac{\rho_{s2}A_{s2}L_1L_2}{T^2}\int_0^1\varphi_{22}^2dx_2+\tfrac{\rho_pA_pL_1L_2}{T^2}\int_0^{\frac{L_p}{L_2}}\varphi_{22}^2dx_2\\&+\tfrac{M_{t1}L_1}{T^2}\varphi_{12}^2(1)+\tfrac{I_{t1}}{L_1T^2}{\varphi'_{12}}^2(1)+\tfrac{M_{t2}L_1}{T^2}\varphi_{22}^2(1)+\tfrac{I_{t2}L_1}{L_2^2T^2}{\varphi'_{22}}^2(1),\\d_3={}&\tfrac{2\rho_{s1}A_{s1}L_1^2}{T^2}\int_0^1\varphi_{11}\varphi_{12}dx_1+\tfrac{\rho_{s2}A_{s2}L_1L_2}{T^2}\int_0^1\varphi_{21}\varphi_{22}dx_2\\&+\tfrac{\rho_pA_pL_1L_2}{T^2}\int_0^{\frac{L_p}{L_2}}\varphi_{21}\varphi_{22}dx_2+\tfrac{M_{t1}L_1}{T^2}\varphi_{11}(1)\varphi_{12}(1)+\tfrac{I_{t1}}{L_1T^2}\varphi'_{11}(1)\varphi'_{12}(1)\\&+\tfrac{M_{t2}L_1}{T^2}\varphi_{21}(1)\varphi_{22}(1)+\tfrac{I_{t2}L_1}{L_2^2T^2}\varphi'_{21}(1)\varphi'_{22}(1),\\\left(B_{s1},C_{s1}\right)={}&b_{s1}\int_{-\frac{h_{s1}}{2}}^{\frac{h_{s1}}{2}}E_s\left(z_1,{z_1}^2\right)dz_1,\\\left(B_{s2},C_{s2}\right)={}&b_{s2}\int_{y_0}^{y_1}E_s\left(z_2,{z_2}^2\right)dz_2,\\\left(B_p\ C_p\right)={}&b_p\int_{y_1}^{y_2}E_p\left(z_2,{z_2}^2\right)dz_2.\end{aligned}\tag{B.2}$$

Supplementary Information The online version contains supplementary material available at https://doi.org/10.1007/s42417-025-01967-7.

Authors'Contributions • Conceptualization: Amir R. Askari.
- Investigation: Yasaman Ghalami and Amir R. Askari
- Methodology: Amir R. Askari
- Software: Yasaman Ghalami and Amir R. Askari
- Validation: Yasaman Ghalami and Amir R. Askari
- Writing - Original Draft: Yasaman Ghalami
- Writing - Review & Editing: Amir R. Askari and Masoud Tahani
- Supervision: Amir R. Askari and Masoud Tahani

Funding The authors did not receive support from any organization for the submitted work.

Data Availability The authors declare that the data supporting the findings of this study are available within the paper.

Declarations

Competing interests The authors have no relevant financial or non-financial interests to disclose.

References

1. Cook-Chennault KA, Thambi N, Sastry AM (2008) Powering MEMS portable devices—a review of non-regenerative and regenerative power supply systems with special emphasis on piezoelectric energy harvesting systems. Smart Mater Struct 17:043001
2. Zhu D, Roberts S, Tudor MJ, Beeby SP (2010) Design and experimental characterization of a tunable vibration-based electromagnetic micro-generator. Sens Actuators A Phys 158:284–293
3. Amin Karami M, Inman DJ (2012) Powering pacemakers from heartbeat vibrations using linear and nonlinear energy harvesters. Appl Phys Lett. https://doi.org/10.1063/1.3679102

4. Kang MG, Jung WS, Kang CY, Yoon SJ (2016) Recent progress on PZT based piezoelectric energy harvesting technologies. Actuators 5:5
5. Elvin NG, Elvin AA (2011) An experimentally validated electromagnetic energy harvester. J Sound Vib 330:2314–2324
6. Khan FU, Qadir MU (2016) State-of-the-art in vibration-based electrostatic energy harvesting. J Micromech Microeng 26:103001
7. Daqaq MF, Masana R, Erturk A, Dane Quinn D (2014) On the role of nonlinearities in vibratory energy harvesting: a critical review and discussion. Appl Mech Rev 66:040801
8. Su WJ, Zu J, Zhu Y (2014) Design and development of a broadband magnet-induced dual-cantilever piezoelectric energy harvester. J Intell Mater Syst Struct 25:430–442
9. Leland ES, Wright PK (2006) Resonance tuning of piezoelectric vibration energy scavenging generators using compressive axial preload. Smart Mater Struct 15:1413
10. Le Scornec J, Guiffard B, Seveno R, Le Cam V (2020) Frequency tunable, flexible and low cost piezoelectric micro-generator for energy harvesting. Sens Actuators A Phys 312:112148
11. Wickenheiser A, Garcia E (2010) Broadband vibration-based energy harvesting improvement through frequency up-conversion by magnetic excitation. Smart Mater Struct 19:065020
12. Zhang J, Qin L (2019) A tunable frequency up-conversion wideband piezoelectric vibration energy harvester for low-frequency variable environment using a novel impact-and rope-driven hybrid mechanism. Appl Energy 240:26–34
13. Farokhi H, Gholipour A, Ghayesh MH (2020) Efficient broadband vibration energy harvesting using multiple piezoelectric bimorphs. J Appl Mech 87:041001
14. Huang X, Zhang C, Dai K (2021) A multi-mode broadband vibration energy harvester composed of symmetrically distributed u-shaped cantilever beams. Micromachines 12:203
15. Abdelkefi A, Barsallo N (2014) Comparative modeling of low-frequency piezomagnetoelastic energy harvesters. J Intell Mater Syst Struct 25:1771–1785
16. Leadenham S, Erturk A (2014) M-shaped asymmetric nonlinear oscillator for broadband vibration energy harvesting: harmonic balance analysis and experimental validation. J Sound Vib 333:6209–6223
17. Tang Y, Wang G, Yang T, Ding Q (2023) Nonlinear dynamics of three-directional functional graded pipes conveying fluid with the integration of piezoelectric attachment and nonlinear energy sink. Nonlinear Dyn 111:2415–2442
18. Gao C, Tang Y, Yang T (2024) Nonlinear dynamics of energy harvesting system for cantilevered fluid-conveying pipes with stopper. Nonlinear Dyn 112:18767–18805
19. Shahruz S (2006) Design of mechanical band-pass filters for energy scavenging. J Sound Vib 292:987–998
20. Xue H, Hu Y, Wang Q-M (2008) Broadband piezoelectric energy harvesting devices using multiple bimorphs with different operating frequencies. IEEE Trans Ultrason Ferroelectr Freq Control 55:2104–2108
21. Ou Q, Chen X, Gutschmidt S, Wood A, Leigh N, Arrieta AF (2012) An experimentally validated double-mass piezoelectric cantilever model for broadband vibration–based energy harvesting. J Intell Mater Syst Struct 23:117–126
22. Erturk A, Renno JM, Inman DJ (2009) Modeling of piezoelectric energy harvesting from an L-shaped beam-mass structure with an application to UAVs. J Intell Mater Syst Struct 20:529–544
23. Kim I-H, Jung H-J, Lee BM, Jang S-J (2011) Broadband energy-harvesting using a two degree-of-freedom vibrating body. Appl Phys Lett. https://doi.org/10.1063/1.3595278
24. Wu H, Tang L, Yang Y, Soh CK (2013) A novel two-degrees-of-freedom piezoelectric energy harvester. J Intell Mater Syst Struct 24:357–368
25. Li X, Yu K, Upadrashta D, Yang Y (2019) Multi-branch sandwich piezoelectric energy harvester: Mathematical modeling and validation. Smart Mater Struct 28:035010
26. Stanton SC, McGehee CC, Mann BP (2010) Nonlinear dynamics for broadband energy harvesting: investigation of a bistable piezoelectric inertial generator. Physica D Nonlinear Phenom 239:640–653
27. Erturk A, Inman DJ (2011) Broadband piezoelectric power generation on high-energy orbits of the bistable Duffing oscillator with electromechanical coupling. J Sound Vib 330:2339–2353
28. Pellegrini SP, Tolou N, Schenk M, Herder JL (2013) Bistable vibration energy harvesters: a review. J Intell Mater Syst Struct 24:1303–1312
29. Harne RL, Wang K (2013) A review of the recent research on vibration energy harvesting via bistable systems. Smart Mater Struct 22:023001
30. Zhou S, Cao J, Inman DJ, Lin J, Liu S, Wang Z (2014) Broadband tristable energy harvester: modeling and experiment verification. Appl Energy 133:33–39
31. Kim P, Seok J (2014) A multi-stable energy harvester: dynamic modeling and bifurcation analysis. J Sound Vib 333:5525–5547
32. Zhou Z, Qin W, Zhu P (2016) Improve efficiency of harvesting random energy by snap-through in a quad-stable harvester. Sens Actuators A Phys 243:151–158
33. Zhou S, Cao J, Erturk A, Lin J (2013) Enhanced broadband piezoelectric energy harvesting using rotatable magnets. Appl Phys Lett. https://doi.org/10.1063/1.4803445
34. Zou HX, Zhang WM, Li WB, Hu KM, Wei KX, Peng ZK, Meng G (2017) A broadband compressive-mode vibration energy harvester enhanced by magnetic force intervention approach. Appl Phys Lett. https://doi.org/10.1063/1.4981256
35. Gao Y, Leng Y, Fan S, Lai Z (2014) Performance of bistable piezoelectric cantilever vibration energy harvesters with an elastic support external magnet. Smart Mater Struct 23:095003
36. Leng Y, Gao Y, Tan D, Fan S, Lai Z (2015) An elastic-support model for enhanced bistable piezoelectric energy harvesting from random vibrations. J Appl Phys. https://doi.org/10.1063/1.4907763
37. Nguyen MS, Yoon Y-J, Kwon O, Kim P (2017) Lowering the potential barrier of a bistable energy harvester with mechanically rectified motion of an auxiliary magnet oscillator. Appl Phys Lett. https://doi.org/10.1063/1.4994111
38. Zhou Z, Qin W, Du W, Zhu P, Liu Q (2019) Improving energy harvesting from random excitation by nonlinear flexible bi-stable energy harvester with a variable potential energy function. Mech Syst Signal Process 115:162–172
39. Chen L, Liao X, Sun B, Zhang N, Wu J (2022) A numerical-experimental dynamic analysis of high-efficiency and broadband bistable energy harvester with self-decreasing potential barrier effect. Appl Energy 317:119161
40. Wu H, Tang L, Yang Y, Soh CK (2014) Development of a broadband nonlinear two-degree-of-freedom piezoelectric energy harvester. J Intell Mater Syst Struct 25:1875–1889
41. Zayed AA, Assal SF, Nakano K, Kaizuka T, Fath El-Bab AM (2019) Design procedure and experimental verification of a broadband quad-stable 2-DOF vibration energy harvester. Sensors 19:2893
42. Tian L, Shen H, Yang Q, Song R, Bian Y (2023) A novel outer-inner magnetic two degree-of-freedom piezoelectric energy harvester. Energy Convers Manage 283:116920
43. Erturk A, Inman DJ (2011) Piezoelectric energy harvesting. John Wiley & Sons
44. Xu Z, Shan X, Yang H, Wang W, Xie T (2017) Parametric analysis and experimental verification of a hybrid vibration energy harvester combining piezoelectric and electromagnetic mechanisms. Micromachines 8:189

45. Khaghanifard J, Askari AR, Taghizadeh M, Awrejcewicz J, Folkow PD (2023) Nonlinear modelling of unimorph and bimorph magneto-electro-elastic energy harvesters. Appl Math Model 119:803–830
46. Reddy JN (2006) Theory and analysis of elastic plates and shells. CRC Press
47. Zou HX, Zhang WM, Li WB, Wei KX, Hu KM, Peng ZK, Meng G (2018) Magnetically coupled flextensional transducer for wideband vibration energy harvesting: design, modeling and experiments. J Sound Vib 416:55–79
48. Beeby SP, O'Donnell T (2009) Electromagnetic energy harvesting. In: Priya S, Inman DJ (eds) Energy Harvesting Technologies. Springer, US, Boston, MA, pp 129–161
49. Wang H-y, Tang L-h, Guo Y, Shan X-b, Xie T (2014) A 2DOF hybrid energy harvester based on combined piezoelectric and electromagnetic conversion mechanisms. J Zhejiang Univ Sci A 15:711–722
50. Xu Z, Shan X, Chen D, Xie T (2015) A novel tunable multi-frequency hybrid vibration energy harvester using piezoelectric and electromagnetic conversion mechanisms. Appl Sci 6:10
51. Spreemann D, Hoffmann D, Folkmer B, Manoli Y (2008) Numerical optimization approach for resonant electromagnetic vibration transducer designed for random vibration. J Micromech Microeng 18:104001
52. Chillara V, Ramanathan A, Dapino M (2020) Self-sensing piezoelectric bistable laminates for morphing structures. Smart Mater Struct 29:085008
53. Meirovitch L (2010) Fundamentals of vibrations. Waveland Press
54. Krishnasamy M, Upadrashta D, Yang Y, Lenka TR (2018) Distributed parameter modelling of cutout 2-DOF cantilevered piezo-magneto-elastic energy harvester. J Microelectromech Syst 27:1160–1170